
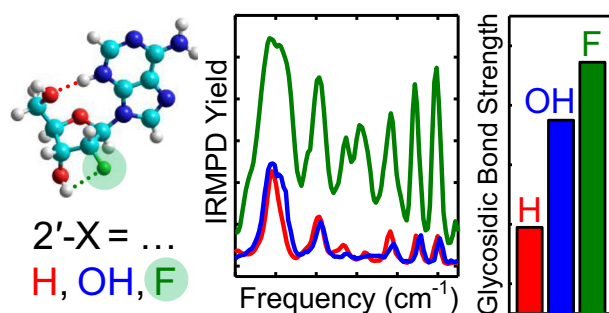


Structures and Relative Glycosidic Bond Stabilities of Protonated 2'-Fluoro-Substituted Purine Nucleosides

Zachary J. Devereaux,¹ C. C. He,¹ Y. Zhu,¹ H. A. Roy,¹ N. A. Cunningham,¹ L. A. Hamlow,¹ G. Berden,² J. Oomens,² M. T. Rodgers¹ 

¹Department of Chemistry, Wayne State University, 5101 Cass Avenue, Detroit, MI 48202, USA

²Institute for Molecules and Materials, FELIX Laboratory, Radboud University, Toernooiveld 7c, 6525 ED, Nijmegen, The Netherlands



Abstract. The 2'-substituent is the primary distinguishing feature between DNA and RNA nucleosides. Modifications to this critical position, both naturally occurring and synthetic, can produce biologically valuable nucleoside analogues. The unique properties of fluorine make it particularly interesting and medically useful as a synthetic nucleoside modification. In this work, the effects of 2'-fluoro modification on the protonated gas-phase purine nucleosides are examined

using complementary tandem mass spectrometry and computational methods. Direct comparisons are made with previous studies on related nucleosides. Infrared multiple photon dissociation action spectroscopy performed in both the fingerprint and hydrogen-stretching regions allows for the determination of the experimentally populated conformations. The populated conformers of protonated 2'-fluoro-2'-deoxyadenosine, [Adofl+H]⁺, and 2'-fluoro-2'-deoxyguanosine, [Guofl+H]⁺, are highly parallel to their respective canonical DNA and RNA counterparts. Both N3 and N1 protonation sites are accessed by [Adofl+H]⁺, stabilizing *syn* and *anti* nucleobase orientations, respectively. N7 protonation and *anti* nucleobase orientation dominates in [Guofl+H]⁺. Spectroscopically observable intramolecular hydrogen-bonding interactions with fluorine allow more definitive sugar puckering determinations than possible for the canonical systems. [Adofl+H]⁺ adopts C2'-endo sugar puckering, whereas [Guofl+H]⁺ adopts both C2'-endo and C3'-endo sugar puckering. Energy-resolved collision-induced dissociation experiments with survival yield analyses provide relative glycosidic bond stabilities. The *N*-glycosidic bond stabilities of the protonated 2'-fluoro-substituted purine nucleosides are found to exceed those of their canonical analogues. Further, the *N*-glycosidic bond stability is found to increase with increasing electronegativity of the 2'-substituent, i.e., H < OH < F. The *N*-glycosidic bond stability is also greater for the adenine nucleoside analogues than the guanine nucleoside analogues.

Keywords: Modified purine nucleosides, Fluorinated nucleoside analogues, Energy-resolved collision-induced dissociation (ER-CID), Survival yield analysis, Infrared multiple photon dissociation (IRMPD) action spectroscopy, Fluorine hydrogen bond, Free electron laser (FEL), Electronic structure theory

Received: 20 December 2018/Revised: 10 April 2019/Accepted: 10 April 2019/Published Online: 20 May 2019

Electronic supplementary material The online version of this article (<https://doi.org/10.1007/s13361-019-02222-6>) contains supplementary material, which is available to authorized users.

Correspondence to: M. T. Rodgers; e-mail: mrodgers@chem.wayne.edu

Introduction

2'-Deoxyribonucleic acids (DNA) and ribonucleic acids (RNA) are the molecular materials responsible for the coding and decoding of the genetic information of life [1]. These biopolymers consist of long chains of nucleosides attached sequentially via 5'-3' phosphodiester bonds.

Nucleosides consist of a planar, nitrogenous, and aromatic nucleobase and a functionalized five-membered ring sugar. The common purine nucleobases are adenine (Ade) and guanine (Gua), whereas the common pyrimidine nucleobases are cytosine (Cyt), uracil (Ura), and thymine (Thy). The purine and pyrimidine nucleobases are connected to their pentose sugar constituents via C1'-N9 and C1'-N1 glycosidic bonds, respectively. The stability of these *N*-glycosidic bonds is crucial. In some regards, the *N*-glycosidic bond stability must maintain a balance such that it is stable enough to maintain the proper sequence fidelity of DNA and RNA strands, but must also be available for cleavage via various base-excision repair pathways to correct undesirably mutated nucleobases [2–8].

The 2'-deoxyribose sugar constituents of DNA nucleosides (dNuo) have a 2'-hydrogen, whereas the ribose sugar constituents of RNA nucleosides (Nuo) have a 2'-hydroxy group. This difference in the 2'-substituent functionality is the primary characteristic that defines the chemistry and classification of DNA and RNA molecules. Synthetic replacement of the 2'-substituent with fluorine produces the unnatural nucleoside analogues, 2'-fluoro-2'-deoxynucleosides (Nuofl). The pyrimidine Nuofl include 2'-fluoro-2'-deoxycytidine (Cydfl) and 2'-fluoro-2'-deoxyuridine (Urdfl) [9] and the purine Nuofl include 2'-fluoro-2'-deoxyadenosine (Adofl) and 2'-fluoro-2'-deoxyguanosine (Guofl). Fluorine substitutions are among the most commonly pursued and medically useful synthetic modifications to natural products [10–16]. Syntheses of Nuofl and other fluorinated nucleoside derivatives have been continually pursued, improved, and screened for pharmaceutical activity, especially anticancer and antiviral effects, for decades [11, 17–22]. The extensive pharmaceutical applications of fluorine arise from its unique ability to impart significant electronic effects with minimal structural changes to molecules. The very high electronegativity of fluorine [23] affects many critical aspects of potentially therapeutic molecules, including lipophilicity, bond strengths, dipole moments, polarizabilities, and the acidity or basicity of nearby functional groups [12, 24, 25]. 2'-Fluoro modifications to nucleosides are of further fundamental interest due to the unique ability of fluorine to mimic some properties of both hydrogen and hydroxyl groups. For example, fluorine is intermediate in size to hydrogen and hydroxy groups [26]. Additionally, fluorine substituents can accept but not donate hydrogen bonds, whereas hydroxy substituents can both accept and donate hydrogen bonds, and hydrogen substituents cannot do either. The small steric bulk and hydrogen bond accepting ability of fluorine has implications in enzyme binding, where noncovalent interactions are used to guide and stabilize substrates into specific spaces and conformations for subsequent catalyzed chemical reactions [1, 27]. Some fluorinated substrates, such as the 2',2'-difluorinated nucleoside drug gemcitabine [28], display substantially increased enzyme-substrate binding affinities and competitively inhibit the unmodified substrates from entering the enzyme active sites, whereas others, such as 5-fluorouracil [29], display mechanism-based inhibition through the irreversible formation of enzyme-substrate complexes [13, 27, 30]. The occurrence and stability

of H···F interactions in the condensed phase remains a subject of interest and debate [31–38]. Although F has higher electronegativity, H···F hydrogen bonds tend to be approximately half as strong as parallel H···O interactions [25].

The various structures and functions of DNA and RNA strands are ultimately emergent features arising from the makeup of their constituents. The study of the isolated constituents of complex biological systems provides insight into their biochemistry from a “bottom-up” perspective. The solvent-free and controllable chemical environment of tandem mass spectrometry (MS/MS) experiments has proven an invaluable asset in the study of various aspects of the canonical and noncanonical DNA and RNA constituents. For example, energy-resolved collision-induced dissociation (ER-CID) experiments performed under multiple collision conditions in trapping mass spectrometers have been used to study the relative stability of various nucleosides [9, 39–45]. Additionally, threshold analysis of ER-CID experiments performed under nominally single collision conditions on guided ion beam mass spectrometers (GIBMS) have provided thermodynamically accurate dissociation energetics for various noncovalent [46–52] and covalent [53–56] interactions of nucleobases and nucleosides. Infrared multiple photon dissociation (IRMPD) action spectroscopy has been used to determine the experimentally populated structures of many canonical and noncanonical forms of nucleobases [57–66], nucleosides [9, 39–44, 67–74], and nucleotides [75–80].

In this work, two types of MS/MS are utilized complementarily with electronic structure calculations to study the protonated forms of the two purine Nuofl, [Adofl+H]⁺ and [Guofl+H]⁺. The neutral chemical structures of Adofl and Guofl are shown in Figure 1. ER-CID experiments with survival yield analyses provide relative *N*-glycosidic bond stabilities. IRMPD action spectroscopy experiments compared with theoretical IR spectra of low-energy stable structures of these species allows determination of the three-dimensional gas-phase ion conformations populated in the experiments. Comparisons are primarily made between this work and previously reported ER-CID, IRMPD, and computational studies of the protonated 2'-fluoro pyrimidine nucleosides [Nuofl+H]⁺ [9], the protonated canonical RNA nucleosides, [Nuo+H]⁺, and the protonated canonical DNA nucleosides, [dNuo+H]⁺ [42, 43, 55, 56, 70, 71].

Experimental and Theoretical Methods

Materials and Locations

Adofl and Guofl (see Figure 1 for neutral chemical structures) were purchased from Hongene Biotechnology Limited (Morrisville, NC, USA) and used as supplied for ER-CID and IRMPD experiments. ER-CID experiments were performed at Wayne State University (WSU; Detroit, MI, USA). In these experiments, methanol (HPLC grade) and glacial acetic acid were purchased from Fisher Scientific (Waltham, MA, USA), and water (HPLC grade) was purchased from Sigma-Aldrich Corporation (St. Louis, MO, USA). IRMPD action

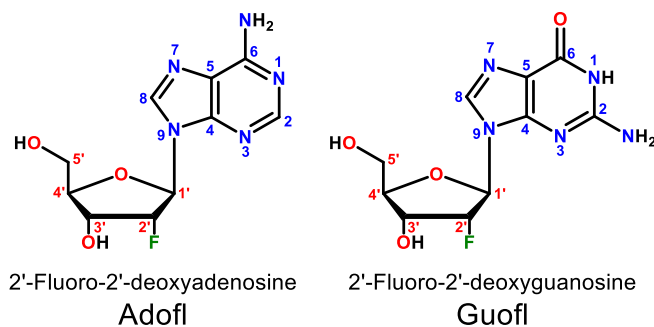


Figure 1. Chemical structures of neutral 2'-fluoro-2'-deoxyadenosine (Adofl) and 2'-fluoro-2'-deoxyguanosine (Guofl). The numbering of the atoms of the nucleobase and sugar moieties are shown

spectroscopy experiments were performed at the FELIX Facility at Radboud University (Nijmegen, The Netherlands). For these experiments, methanol (HPLC grade), water (HPLC grade), and fuming hydrochloric acid were purchased from Sigma-Aldrich Corporation (St. Gallen, Switzerland).

Energy-Resolved Collision-Induced Dissociation

Separate working solutions of the nucleosides Adofl and Guofl were prepared at concentrations of $\sim 10 \mu\text{M}$ in 50/50 methanol/water with $\sim 0.1\%$ acetic acid. These solutions were introduced via mechanical syringe pump at a flow rate of $\sim 3 \mu\text{L}/\text{min}$ to the Apollo II electrospray ionization (ESI) source of an amaZon ETD quadrupole ion trap mass spectrometer (QIT MS; Bruker Corporation, Billerica, MA; Bruker Daltonics, Bremen Germany). The precursor ions, $[\text{Adofl}+\text{H}]^+$ and $[\text{Guofl}+\text{H}]^+$, were transferred via rf ion guides and static lenses to the QIT MS where they were mass isolated. Helium (and background residual gases) present in the trap chamber at a stagnation pressure of $\sim 1 \text{ mTorr}$ was used as the CID collision gas. Mass spectra were collected as a function of the rf excitation amplitude (r_{fEA}) used to excite the ion kinetic energies during CID. The r_{fEA} was ramped from 0.00 V to a value beyond that required to achieve 100% precursor ion dissociation ($\sim 0.6 \text{ V}$ maximum for the systems studied here) in steps of 0.01 V per 30 s segments. The r_{fEA} was applied for 40 ms during each MS/MS sequence. With the experimental sequence employed, ~ 50 spectra were collected and averaged at each r_{fEA} during each ER-CID scan. Experiments were performed in triplicate. Compass Data Analysis 4.0 software (Bruker Daltonics, Bremen, Germany) was used to acquire, extract, and export the mass spectral data. Custom software developed in our laboratory was used to extract time-resolved raw intensity data from the Bruker data files and calculate r_{fEA} -dependent survival yields according to Eq. (1):

$$\text{Survival yield} = I_{\text{p}} / (I_{\text{f}} + I_{\text{p}}) \quad (1)$$

where I_{p} and I_{f} are the precursor and fragment ion intensities, respectively. The survival yield data was fit with a four-parameter logistic dynamic curve as shown in Eq. (2):

$$\text{Survival yield} = \min + \left\{ (\max - \min) / \left(1 + \frac{r_{\text{fEA}}^{\text{CID}_{50\%}}}{\text{CID}_{50\%}^{\text{slope}}} \right) \right\} \quad (2)$$

where max is the maximum possible value, set to 1 here and corresponding to precursor isolation without fragmentation; min is the minimum possible value, set to 0 here and corresponding to complete precursor ion dissociation; $\text{CID}_{50\%}^{\text{slope}}$ is the slope of the declining region of the survival yield curve; and the $\text{CID}_{50\%}$ value is the r_{fEA} required to give a survival yield of 50%. The $\text{CID}_{50\%}$ value is extracted from this fit and used as a relative measurement of *N*-glycosidic bond stability. SigmaPlot Version 10.0 (Systat Software, Inc., San Jose, CA, USA) was used to fit, analyze, and plot the data.

Infrared Multiple Photon Dissociation Action Spectroscopy

Separate working solutions of the nucleosides Adofl and Guofl were prepared at concentrations of $\sim 1 \text{ mM}$ in 50/50 methanol/water with $\sim 0.1\%$ hydrochloric acid. These solutions were introduced via mechanical syringe pump at a flow rate of $\sim 5 \mu\text{L}/\text{min}$ to the “Z-Spray” ESI source (Micromass, Milford, MA, USA) of a homebuilt 4.7 T Fourier transform ion cyclotron resonance mass spectrometer (FT-ICR MS). This FT-ICR MS is coupled with two sources of tunable infrared (IR) laser light: the free electron laser for infrared experiments (FELIX) [81, 82] and a benchtop optical parametric oscillator/optical parametric amplifier (OPO) laser system (LaserVision, Bellevue, WA, USA States) [74, 83] pumped by an InnoLas SpitLight 600 Nd:YAG (Krailling, Germany). The precursor ions, $[\text{Adofl}+\text{H}]^+$ and $[\text{Guofl}+\text{H}]^+$, were accumulated and thermalized in a hexapole ion trap and then pulsed through a quadrupole bender and injected into the ICR cell where they were trapped and mass isolated using stored waveform inverse Fourier transform (SWIFT) techniques. The isolated precursor ions were then irradiated with IR light from either FELIX or the OPO. With absorption of a sufficient number of resonant photons, the ion internal energies may reach or exceed their dissociation energy thresholds and fragment. IRMPD yields were calculated as a function of laser wavelength using Eq. (3):

$$\text{IRMPD yield} = I_{\text{f}} / (I_{\text{f}} + I_{\text{p}}) \quad (3)$$

where I_{f} and I_{p} are defined as in Eq. (1). FELIX was operated at 5 Hz, and the $[\text{Adofl}+\text{H}]^+$ and $[\text{Guofl}+\text{H}]^+$ ions were irradiated for 3.0 and 3.5 s, respectively, over the vibrational frequency range of $\sim 600\text{--}1850 \text{ cm}^{-1}$. The OPO was operated at 10 Hz, and the $[\text{Adofl}+\text{H}]^+$ and $[\text{Guofl}+\text{H}]^+$ ions were irradiated for 7.5 s over the vibrational frequency range of $\sim 3300\text{--}3800 \text{ cm}^{-1}$. IRMPD yields were normalized linearly based on the irradiation time length and a least squares fit of the laser power as a function of wavelength.

Computational Approaches

The molecular structures and atom numbering for neutral Adofl and Guofl are shown in Figure 1. Potentially favorable

protonation sites of these nucleosides were investigated. For Adofl, this included protonation at the N1, F2', N3, and N7 positions. For Guofl, this included protonation at the F2', N3, O6, and N7 positions. Candidate structures were generated for each protonated nucleoside form via a molecular dynamics simulated annealing procedure using the HyperChem software (Hypercube, Inc., Gainesville, FL, USA) and the Amber 3 force field. During simulated annealing, the ion was heated from 0 to 1000 K over 0.3 ps, conformational space was sampled at 1000 K for 0.2 ps, and the ion was cooled from 1000 to 0 K over 0.3 ps. A snapshot of the resulting structure was saved and used to initiate the next simulated annealing cycle. This process was repeated 300 times for each of the initial protonated forms of the nucleosides, and ~30 of the most stable conformers from each simulated annealing run were subjected to density functional theory (DFT) calculations. The optimized structures previously reported for [Nuo+H]⁺ and [dNuo+H]⁺ along with chemical intuition were used to generate additional conformers to complement those found via simulated annealing in an attempt to comprehensively sample all possible low-energy structures.

The Gaussian 09 suite of programs [84] was used to perform geometry optimizations, frequency analyses, and single-point energy determinations. Geometry optimizations and frequency analyses were performed at the B3LYP/6-311+G(d,p) level of theory at standard ambient temperature and pressure and with a frequency scaling factor of 0.9887 [85]. Theoretical linear IR spectra were generated by the software and scaled by factors of 0.980 and 0.957 in the ~600–1850 cm⁻¹ fingerprint and ~3300–3800 cm⁻¹ hydrogen-stretching regions, respectively, for both [Adofl+H]⁺ and [Guofl+H]⁺. The predicted linear IR spectra were broadened using 30 cm⁻¹ and 15 cm⁻¹ full width at half maximum (FWHM) Gaussian line shapes for the fingerprint and hydrogen-stretching regions, respectively. Single-point energy determinations were performed at the B3LYP/6-311+G(2d,2p) and MP2(full)/6-311+G(2d,2p) levels of theory for each optimized structure. Additional single point energy calculations at the B3LYP/6-311+G(2d,2p) and MP2(full)/6-311+G(2d,2p) levels of theory were performed for selected conformers using the polarizable continuum model (PCM) with an implicit water solvent. Zero-point energy (ZPE) and thermal corrections at 298 K were included in the relative stabilities computed.

Conformer Designations and Structural Characterizations

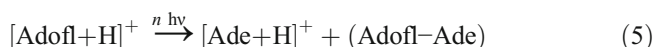
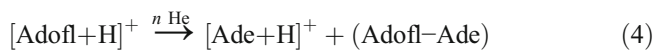
Comparisons between the experimental IRMPD and predicted linear IR spectra allow for the inclusion or exclusion of calculated conformers as being present as gas-phase ions in the MS experiments. Calculated conformers are named based on their site of protonation followed by a letter incremented alphabetically based on their relative B3LYP/6-311+G(2d,2p) Gibbs energy at 298 K. GaussView 5.0 (Gaussian, Inc., Wallingford, CT, USA) was used to extract bond lengths and angles. Structural descriptions are made according to methods described in detail in previous work

[39–43, 86–88] and described briefly here. Purine nucleobase orientations are classified as *anti* or *syn* as defined by ∠C4N9C1'O4' dihedral angle ranges of -90° to 90° and 90° to 270°, respectively. Sugar puckers are described in two ways. In the first classification scheme, descriptors are given to the sugar ring atom that deviates the greatest distance from the plane formed by the other four sugar ring atoms. Endo configurations deviate toward the 5'-hydroxyl, whereas exo configurations deviate away. In the second classification scheme, more descriptive designations based on the pseudorotation angle (*P*^o) of the sugar are used. *P*^o is calculated using the five dihedral angles of the sugar moiety. Envelope (E) structures have only one atom deviating from the plane of the sugar, whereas twist (T) structures have two atoms deviating in opposite directions. Superscripted numbers indicate endo configurations, whereas subscripts represent exo. The number prior to the letter designation (E or T) indicates the atom number of the major deviator from the sugar plane, whereas the number after the letter indicates the atom number of the minor deviator.

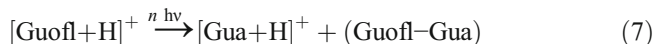
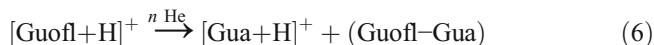
Results and Discussion

CID and IRMPD Dissociation Pathways

Both CID, when performed in a QIT MS, and IRMPD are multi-step, slow-heating processes [89–92]. Activation of [Adofl+H]⁺ by multiple collisions, Eq. (4), and multiple IR photons, Eq. (5), produces the same reaction products.



In both reactions, [Adofl+H]⁺ solely dissociates via *N*-glycosidic bond cleavage to produce the protonated adenine nucleobase [Ade+H]⁺ and the corresponding neutral sugar moiety (Adofl–Ade). Similarly, activation of [Guofl+H]⁺ by multiple collisions, Eq. (6), and multiple IR photons, Eq. (7), also produces parallel reaction products.



In both of these reactions, [Guofl+H]⁺ solely dissociates via *N*-glycosidic bond cleavage to produce the protonated guanine nucleobase [Gua+H]⁺ via neutral loss of the corresponding neutral 2'-fluorinated sugar moiety (Guofl–Gua).

CID MS/MS spectra for [Adofl+H]⁺ and [Guofl+H]⁺ acquired at an *r*_{FEA} near their CID_{50%} value are shown in Figure 2. Previously published [39, 40] MS/MS spectra for [Ado+H]⁺, [dAdo+H]⁺, [Guo+H]⁺, and [dAdo+H]⁺ are also included in Figure 2 for comparison. The *N*-glycosidic bond cleavage

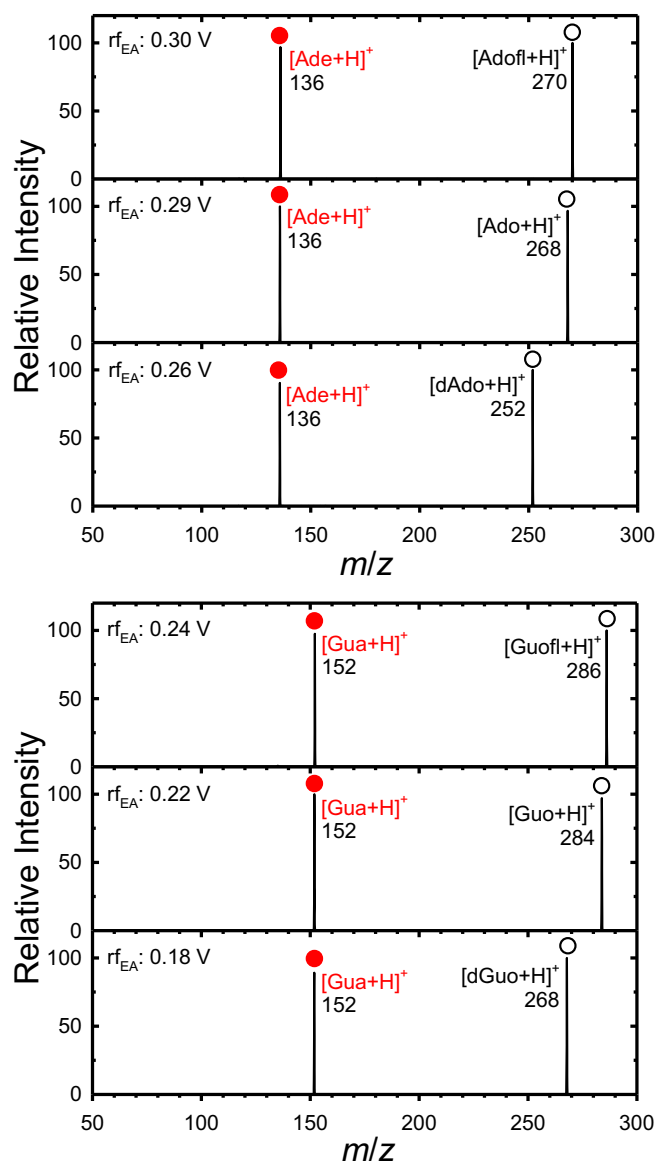


Figure 2. CID MS/MS spectra acquired at rf excitation amplitudes (rf_{EA}) that produced $\sim 50\%$ dissociation of $[Adofl+H]^+$, $[Ado+H]^+$, and $[dAdo+H]^+$ (top panel) and $[Guofl+H]^+$, $[Guo+H]^+$, and $[dGuo+H]^+$ (bottom panel). Results for the protonated canonical RNA and DNA nucleosides were taken from previous work [39, 40]

pathways observed for $[Adofl+H]^+$ and $[Guofl+H]^+$ exactly parallel those found for their canonical DNA and RNA forms: $[dAdo+H]^+$, $[dGuo+H]^+$, $[Ado+H]^+$, and $[Guo+H]^+$ [39, 40, 53, 54, 67, 68], as well as for the protonated noncanonical purine 2'-O-methylnucleosides, $[Adom+H]^+$ and $[Guom+H]^+$ [44], and other protonated and sodium cationized noncanonical methylguanosines [45]. The pyrimidine $[Nuofl+H]^+$, $[Nuo+H]^+$, and $[dNuo+H]^+$ also primarily undergo N -glycosidic bond cleavage [41–43, 69–71]; however, several competing neutral loss pathways are also observed for the protonated uracil and thymine nucleoside analogues.

Relative Stability Comparisons

With judicious employment of QIT MS ER-CID and survival yield analyses, the relative stability of ions can be determined [9, 44, 45, 92–99]. Figure 3 compares survival yield curves for $[Adofl+H]^+$, $[Ado+H]^+$, $[dAdo+H]^+$, $[Guofl+H]^+$, $[Guo+H]^+$, and $[dGuo+H]^+$. The $[Adofl+H]^+$ and $[Guofl+H]^+$ results were acquired in this work, whereas data for $[Ado+H]^+$, $[dAdo+H]^+$, $[Guo+H]^+$, and $[dGuo+H]^+$ are reproduced from previous work [40]. With the comparable conditions and reaction pathways observed in the experiments, the $CID_{50\%}$ values of these protonated nucleosides can be understood and compared as a measure of the relative stability of their N -glycosidic bonds.

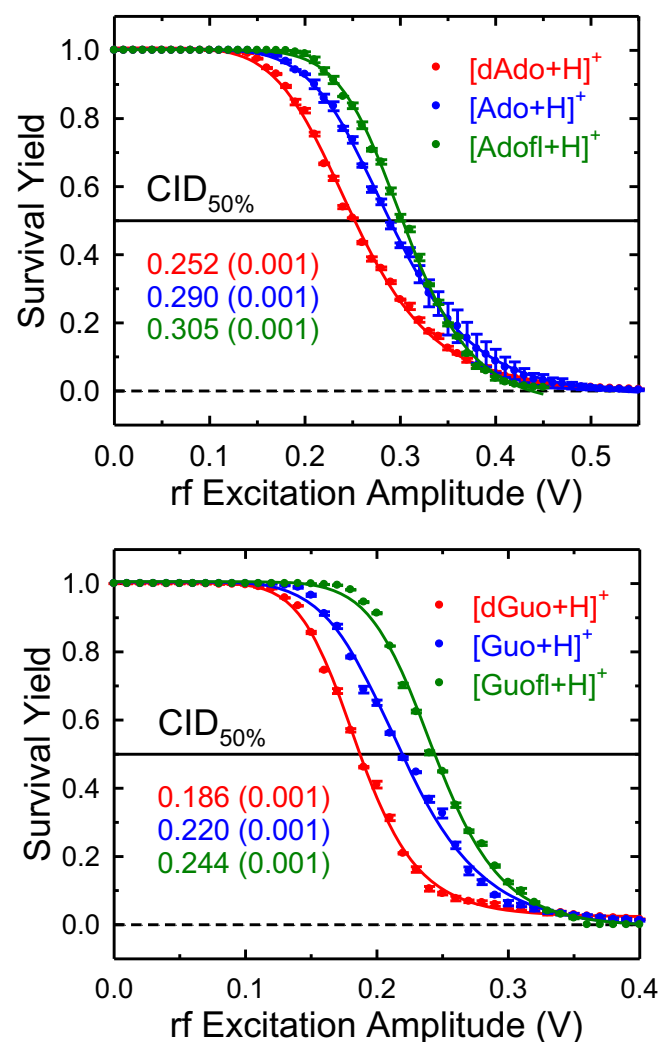


Figure 3. Survival yield curves for $[Adofl+H]^+$, $[Ado+H]^+$, and $[dAdo+H]^+$ (top panel) and $[Guofl+H]^+$, $[Guo+H]^+$, and $[dGuo+H]^+$ (bottom panel). Error bars represent one standard deviation of the data measured in triplicate. Fits to the survival yield measurements using a dynamic four-parameter logistic curve, the extracted $CID_{50\%}$ values, and the standard error associated with the fit (in parentheses) are shown. Survival yield data for the protonated canonical RNA and DNA nucleosides were taken from previous work [39, 40]

Two important trends are observed in the data. First, the *N*-glycosidic bond stability is observed to vary with the 2'-substituent. The $CID_{50\%}$ values of $[dAdo+H]^+$, $[Ado+H]^+$, and $[Adofl+H]^+$ increase from 0.252 ± 0.001 to 0.290 ± 0.001 to 0.305 ± 0.001 V, respectively. Similar behavior is seen in the $CID_{50\%}$ values of $[dGuo+H]^+$, $[Guo+H]^+$, and $[Guofl+H]^+$, which increase from 0.186 ± 0.001 to 0.220 ± 0.001 to 0.244 ± 0.001 V, respectively. Parallel trends regarding the influence of the 2'-substituent on the glycosidic bond stability of the protonated pyrimidine nucleosides were also found [9]. These results can be explained by examining the electronegativities of the 2'-substituents, which follow that same order: 2'-H (2.20) < 2'-OH (3.44) < 2'-F (3.98) [23, 100]. Increasing electronegativity of the 2'-substituent draws more electron density from the 2'-C, giving it greater partial positive character. This partial positive character destabilizes the proposed oxocarbenium ion intermediate [53–56, 101, 102] and increases the energy necessary to activate the glycosidic bond. The second trend relates to the identity of the nucleobases. For the purine nucleobases, the adenine nucleoside analogues exhibit greater glycosidic bond strength than the guanine nucleoside analogues. Figure S1 compares the survival yield curves of $[Adofl+H]^+$ and $[Guofl+H]^+$ with previously published [9] results for $[Cydfl+H]^+$ and $[Urdfl+H]^+$. From this data, the relative glycosidic bond stabilities of the $[Nuofl+H]^+$ increase with the trend: $[Urdfl+H]^+ < [Cydfl+H]^+ < [Guofl+H]^+ < [Adofl+H]^+$ (respective $CID_{50\%}$ values, 0.213 ± 0.001 V < 0.224 ± 0.001 V < 0.244 ± 0.001 V < 0.305 ± 0.001 V). Parallel trends as a function of nucleobase were observed in the previously studied $[Nuo+H]^+$ and $[dNuo+H]^+$ systems [39–43]. These results indicate that the purine nucleoside analogues have a greater glycosidic bond stability than the pyrimidine nucleoside analogues and that the glycosidic bond stabilities increase from the uracil to the cytosine to the guanine to the adenine nucleoside analogues.

IRMPD Action Spectra

Figure 4 displays the IRMPD action spectrum of $[Adofl+H]^+$ compared with the previously published $[Ado+H]^+$ and $[dAdo+H]^+$ spectra [67]. The spectral features of the three IRMPD spectra are overall highly parallel, suggesting similar structural conformations. Table 1 shows the vibrational band assignments for the $[Adofl+H]^+$ spectrum based on the experimentally populated conformers determined in this work. In the fingerprint region, from ~ 550 to 1850 cm^{-1} , the primary change between the $[Adofl+H]^+$ spectrum and the canonical $[Ado+H]^+$ and $[dAdo+H]^+$ spectra is an increase in the relative intensities of the absorption bands, especially between ~ 1150 – 1650 cm^{-1} and ~ 600 – 1000 cm^{-1} . Modest peak broadening and absorption intensity changes are observed in the ~ 1575 – 1725 cm^{-1} , ~ 1350 – 1550 cm^{-1} , and ~ 1000 – 1150 cm^{-1} regions. In the hydrogen-stretching region, from ~ 3300 – 3750 cm^{-1} , the primary spectral difference is the splitting of the ~ 3668 cm^{-1} band corresponding to the O3'-H and O5'-H stretches in the $[Ado+H]^+$ and

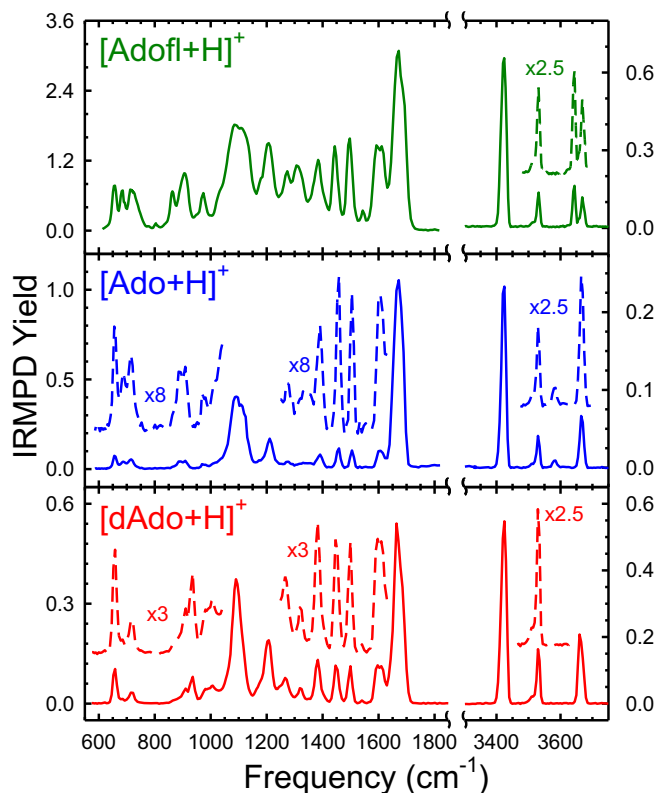


Figure 4. Experimental IRMPD action spectra of $[Adofl+H]^+$, $[Ado+H]^+$, and $[dAdo+H]^+$. Data for the protonated canonical DNA and RNA nucleosides were taken from previous work [67]

$[dAdo+H]^+$ spectra into two distinct O–H stretches at 3644 and 3668 cm^{-1} in the $[Adofl+H]^+$ spectrum. The additional peak at 3644 cm^{-1} is observed due to red shifting of the O3'-H stretch resulting from a hydrogen-bonding interaction with the highly electronegative 2'-F substituent. An additional band at ~ 3580 cm^{-1} is observed in the $[Ado+H]^+$ spectrum that arises from the 2'-O–H stretch, a feature not present in the $[Adofl+H]^+$ and $[dAdo+H]^+$ spectra as this substituent is absent in these nucleosides. The absorption bands corresponding to N–H stretches are highly parallel between the $[Adofl+H]^+$, $[Ado+H]^+$, and $[dAdo+H]^+$ spectra.

Figure 5 displays the IRMPD action spectrum of $[Guofl+H]^+$ compared with the previously published spectra of $[Guo+H]^+$ and $[dGuo+H]^+$ [68]. Table 2 lists the vibrational band assignments for the $[Guofl+H]^+$ spectrum. Again, the spectral features of the three experimental IRMPD spectra are overall highly parallel, suggesting similar structures. In the fingerprint region, the primary change between the $[Guofl+H]^+$ spectrum and the canonical $[Guo+H]^+$ and $[dGuo+H]^+$ spectra is an increase in the relative intensities of absorption bands, especially in the ranges ~ 1725 – 1825 cm^{-1} , ~ 1150 – 1550 cm^{-1} , and ~ 600 – 1050 cm^{-1} . Modest peak broadening is found in the $[Guofl+H]^+$ spectrum, as particularly exemplified in the most intense spectral features in the ~ 1725 – 1825 cm^{-1} , ~ 1550 – 1700 cm^{-1} , and ~ 1050 – 1300 cm^{-1} regions. In the hydrogen-stretching region, $[Guofl+H]^+$ again displays a greater number of absorption bands than its canonical RNA and DNA counterparts. In the $[Guofl+H]^+$ spectrum, two red-shifted bands arise at

Table 1. Vibrational Band Assignments for [Adofl+H]⁺

Vibrational frequency (cm ⁻¹)	N3A	N1A
3668	O5'-H stretch	O5'-H stretch
3644	O3'-H stretch	O3'-H stretch
3532	N6H ₂ antisymmetric stretch	N6H ₂ antisymmetric stretch
3424	N6H ₂ symmetric stretch	N1-H stretch, N6H ₂ symmetric stretch
1693	–	C6–N6 stretch
1665	C6–N6 stretch, N6H ₂ scissor	–
1611	N1–H rock	N6H ₂ scissor
~1600–1450	nucleobase breathing, C–H/O–H/N–H vibrations	nucleobase breathing, C–H/O–H/N–H vibrations
~1450–600	sugar ring breathing, C–H/O–H/N–H vibrations	sugar ring breathing, C–H/O–H/N–H vibrations

Vibrational band assignments are based on the predicted IR spectra for the N3A and N1A conformers

3644 and 3624 cm⁻¹ from O3'-H stretches associated with two distinct O3'H...F geometries among the conformers populated, whereas in the [Guo+H]⁺ and [dGuo+H]⁺ spectra, the O3'-H stretch coalesces with the O5'-H stretch at ~3665 cm⁻¹. The number and position of the N–H, NH₂ symmetric, and NH₂ antisymmetric stretches are consistent among [Guofl+H]⁺, [Guo+H]⁺, and [dGuo+H]⁺, but the relative intensity of the bands at 3564 and 3536 cm⁻¹ is reduced for [Guofl+H]⁺ compared to its canonical counterparts.

The wavelength-dependent IRMPD yields of [Adofl+H]⁺ and [Guofl+H]⁺ and their canonical RNA and DNA forms are overlaid for more direct comparison in Figure S2. Despite their greater glycosidic bond stability, the [Nuofl+H]⁺ nucleosides

exhibit greater IRMPD yields than their canonical forms. The large IRMPD yields of [Nuofl+H]⁺ likely arise from increased IR photon absorption cross sections due to the increased interatom dipole moments in the sugar moiety (see Figure S3) and the lone pairs of the highly electronegative 2'-F substituent. The slightly broader peaks in the [Nuofl+H]⁺ IRMPD spectra are also likely due to the greater absorption cross sections, and therefore the increased absorption band intensities, in the protonated 2'-fluoro-substituted nucleosides compared to the canonical systems. However, minor differences in laser beam profiles from day-to-day, i.e., the shape of the beam about the central frequency, could also lead to differences in absorption peak widths.

B3LYP vs. MP2(full) Stability Comparisons

Previous experimental and theoretical works, especially those reported by Wu et al. and Zhu et al., have determined that single-point energy calculations at the B3LYP/6-311+G(2d,2p) are robust and satisfactory for describing canonical and modified nucleosides [39–43, 53–56, 67–71]. The MP2(full)/6-311+G(2d,2p) level of theory has also proven useful in providing ancillary insight into the conformer energetics for some systems. However, the MP2(full) results consistently mirror the B3LYP results (see Table 3 and Figures S4 and S5) for [Adofl+H]⁺ and [Guofl+H]⁺. Additionally, the [Nuofl+H]⁺ energetics are highly parallel to those calculated for analogous [Nuo+H]⁺ and [dNuo+H]⁺ structures. Therefore, throughout this work, the B3LYP/6-311+G(2d,2p) calculated values will be used in all discussions, and the MP2(full)/6-311+G(2d,2p) values are included in tables and figures for additional reference.

Calculated [Adofl+H]⁺ and [Guofl+H]⁺ Conformers

Unique conformers calculated for [Adofl+H]⁺ are shown in Figure S4. Energetic and structural information for selected conformations (N3A, N3B, N1A, and N7A) is provided in Tables 3 and 4. The ground-state conformation, N3A, has a *syn* nucleobase orientation and C2'-endo (²T₁) sugar puckering. The N3 proton aids in stabilization of the *syn* nucleobase orientation by participating in an N3H⁺...O5' ionic hydrogen-bonding interaction. The C2'-endo (²T₁) sugar pucker is stabilized by an O3'H...F interaction. The N3B conformer lies

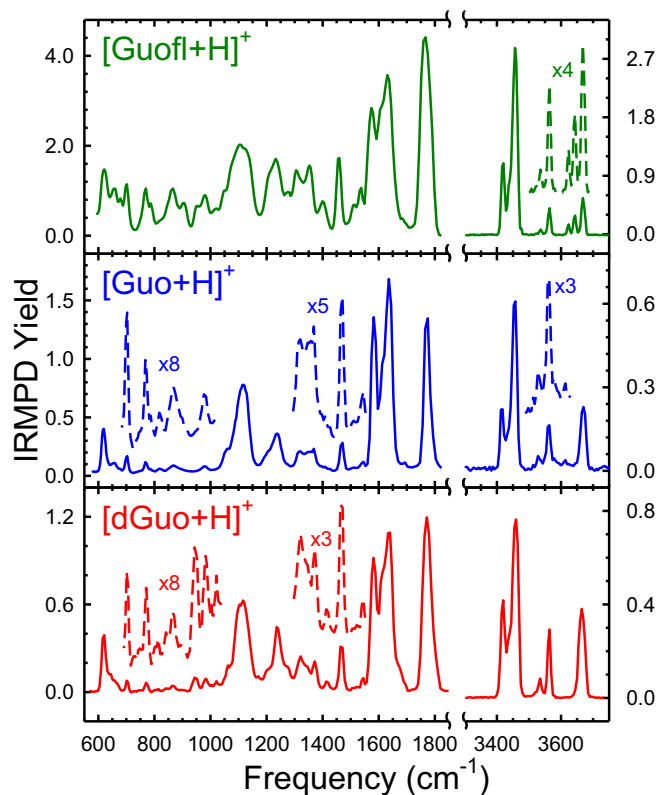


Figure 5. Experimental IRMPD action spectra of [Guofl+H]⁺, [Guo+H]⁺, and [dGuo+H]⁺. Data for the protonated canonical DNA and RNA nucleosides were taken from previous work [68]

Table 2. Vibrational Band Assignments for [Guofl+H]⁺

Vibrational frequency (cm ⁻¹)	N7A	N7B	O6A
3668	O5'-H stretch	O5'-H stretch	O5'-H stretch
3644	–	O3'-H stretch	O3'-H stretch
3624	O3'-H stretch	–	–
3564	N2H ₂ antisymmetric stretch	N2H ₂ antisymmetric stretch	N2H ₂ antisymmetric stretch
3536	–	–	O6-H ⁺ stretch
3456	N2H ₂ symmetric stretch, N7-H ⁺ stretch	N2H ₂ symmetric stretch, N7-H ⁺ stretch	N2H ₂ symmetric stretch
3420	N1-H stretch	N1-H stretch	N1-H stretch
1767	C6=O stretch	C6=O stretch	–
1685	–	–	C5=C6/C2=N3 stretch, O6-H rock
1631	N2H ₂ scissor	N2H ₂ scissor	N2H ₂ scissor, N1-H rock
1611	C4=C5 stretch	C4=C5 stretch	N1-C6/N3-C4 stretch
1573	C2-N3 stretch, N1-H rock, N2H ₂ scissor	C2-N3 stretch, N1-H rock, N2H ₂ scissor	N3-C4 stretch, N2H ₂ scissor
~1550–1350	nucleobase breathing, C-H/O-H/N-H vibrations	nucleobase breathing, C-H/O-H/N-H vibrations	nucleobase breathing, C-H/O-H/N-H vibrations
~1350–600	sugar breathing, C-H/O-H/N-H vibrations	sugar breathing, C-H/O-H/N-H vibrations	sugar breathing, C-H/O-H/N-H vibrations

Vibrational band assignments are based on the predicted IR spectra for the **N7A**, **N7B**, and **O6A** conformers

2.5 kJ/mol higher in B3LYP Gibbs energy, and is highly parallel in structure to **N3A**, except with a C4'-exo (⁴T³) sugar pucker. Disrupting the N3H⁺⋯O5' hydrogen bond of **N3B** produces the **N3C** conformer after optimization at 8.0 kJ/mol B3LYP Gibbs energy, indicating this particular hydrogen-fluorine interaction stabilizes the system by ~5.5 kJ/mol. After N3 protonation, the next most favorable protonation site is at the N1 position. **N1A**, at 20.3 kJ/mol, has an *anti* nucleobase orientation stabilized by a noncanonical C8H⋯O5' hydrogen bond and C2'-endo (²T₃) sugar puckering stabilized by an O3'H⋯F hydrogen bond. **N7A**, the

most stable N7-protonated conformer, lies 35.2 kJ/mol above the ground-state conformation. **N7A** has structural features that are highly parallel to **N1A**, except that rotation of the 3'-hydroxy substituent and thus reorientation of the O3'H⋯F hydrogen bond lead to C3'-endo (³T₂) sugar puckering.

Unique calculated conformers of [Guofl+H]⁺ are shown in Figure S5. Energetic and structural details for selected conformations (**N7A**, **N7B**, **O6A**, and **N3A**) are provided in Tables 3 and 4. The ground-state conformation, **N7A**, has an *anti* nucleobase orientation and C3'-endo (³T₂) sugar puckering.

Table 3. Relative 0 and 298 K Enthalpies and 298 K Gibbs Energies of Selected Low-Energy Conformers of Protonated Purine Nucleoside Analogues

Ion	Conformer	B3LYP			MP2(full)		
		ΔH ₀	ΔH ₂₉₈	ΔG ₂₉₈	ΔH ₀	ΔH ₂₉₈	ΔG ₂₉₈
[Adofl+H] ⁺	N3A	0.0	0.0	0.0	0.0	0.0	0.0
	N3B	3.6	4.0	2.5	6.3	6.6	5.1
	N1A	23.6	25.0	20.3	27.4	28.8	24.1
	N7A	39.0	41.0	35.2	46.2	48.2	42.3
[Guofl+H] ⁺	N7A	0.0	0.0	0.0	0.0	0.0	0.0
	N7B	1.5	1.5	1.4	1.8	1.7	1.7
	O6A	34.5	34.8	33.9	34.0	34.3	33.4
[Ado+H] ⁺	N3A	48.7	48.6	50.4	36.3	36.2	38.0
	N3C	0.0	0.0	0.0	0.0	0.0	0.0
	N1A	25.1	26.5	21.8	28.6	30.0	25.4
	N7A	40.5	42.3	37.2	46.2	48.1	42.9
	N7B	0.9	1.2	0.3	2.1	2.3	1.4
[Guo+H] ⁺	O6A	36.2	36.8	35.0	36.4	36.9	35.2
	N3A	39.4	39.3	41.2	38.4	38.3	40.1
	N3A	0.0	0.0	0.0	0.0	0.0	0.0
	N3B	4.8	5.3	3.6	8.2	8.7	7.0
[dAdo+H] ⁺	N1A	28.5	29.9	25.3	32.5	33.9	29.3
	N7A	37.6	39.7	33.6	45.5	47.6	41.5
	N7A	0.0	0.0	0.0	0.0	0.0	0.0
	N7B	13.7	13.6	14.0	11.6	11.5	11.9
[dGuo+H] ⁺	O6A	39.6	39.8	39.0	38.1	38.3	37.5
	N3A	50.3	49.8	52.4	38.9	38.3	40.9

Energetics based on single-point energy calculations performed at the B3LYP/6-311+G(2d,2p) and MP2(full)/6-311+G(2d,2p) levels of theory with zero-point energy and thermal corrections based on the B3LYP/6-311+G(d,p) optimized structures and vibrational frequencies. Results for [Ado+H]⁺ and [dAdo+H]⁺ were taken from reference [67]. Results for [Guo+H]⁺ and [dGuo+H]⁺ were taken from reference [68]

Table 4. Geometric Parameters of Selected Low-Energy Conformers Computed for Protonated Purine Nucleoside Analogues

Ion	Conformer	Nucleobase orientation	Glycosidic bond length (Å)	Sugar pucker	Hydrogen bond	Hydrogen bond angle (°)	Hydrogen bond length (Å)
[Adofl+H] ⁺	N3A	<i>syn</i>	1.458	C2'-endo (² T ₁)	∠O3'H...F2'	96.0	2.437
					∠N3H ⁺ ...O5'	172.0	1.816
	N3B	<i>syn</i>	1.471	C4'-exo (₄ T ³)	∠O3'H...F2'	107.8	2.261
					∠N3H ⁺ ...O5'	168.2	1.805
[Guofl+H] ⁺	N1A	<i>anti</i>	1.470	C2'-endo (² T ₃)	∠O3'H...F2'	98.2	2.408
					∠O3'H...F2'	106.5	2.305
	N7A	<i>anti</i>	1.495	C3'-endo (³ T ₂)	∠O3'H...F2'	106.1	2.310
					∠O3'H...F2'	97.7	2.410
	N7B	<i>anti</i>	1.479	C2'-endo (² T ₃)	∠O3'H...F2'	97.9	2.410
					∠O3'H...F2'	97.5	2.400
	O6A	<i>anti</i>	1.467	C2'-endo (² T ₃)	∠O3'H...F2'	169.8	1.813
∠O3'H...F2'					114.8	2.105	
N3A	<i>syn</i>	1.455	C2'-endo (² T ₁)	∠N3H ⁺ ...O5'	172.1	1.830	
				∠N3H ⁺ ...O5'	114.4	2.135	
[Ado+H] ⁺	N3A	<i>syn</i>	1.459	C2'-endo (² T ₁)	∠O2'H...O3'	167.5	1.832
					∠N3H ⁺ ...O5'	114.2	2.123
	N3C	<i>syn</i>	1.473	C4'-exo (₄ T ³)	∠O2'H...O3'	114.2	2.160
					∠N3H ⁺ ...O5'	115.3	2.134
[Guo+H] ⁺	N1A	<i>anti</i>	1.470	C2'-endo (² T ₃)	∠O2'H...O3'	113.9	2.125
					∠O2'H...O3'	114.6	2.115
	N7A	<i>anti</i>	1.502	C3'-endo (³ T ₂)	∠O2'H...O3'	113.0	2.186
					∠O2'H...O3'	160.4	1.869
	N7B	<i>anti</i>	1.498	C3'-endo (³ T ₂)	∠N3H ⁺ ...O5'	173.7	1.801
					∠N3H ⁺ ...O5'	169.0	1.803
O6A	<i>anti</i>	1.468	C2'-endo (² T ₃)	–	–	–	
				–	–	–	
N3A	<i>syn</i>	1.472	C4'-exo (₄ T ³)	–	–	–	
				–	–	–	
[dAdo+H] ⁺	N3A	<i>syn</i>	1.465	C2'-endo (² T ₁)	–	–	–
					–	–	–
	N3B	<i>syn</i>	1.479	C4'-exo (₄ T ³)	–	–	–
					–	–	–
N1A	<i>anti</i>	1.479	C2'-endo (² T ₃)	–	–	–	
				–	–	–	
N7A	<i>anti</i>	1.512	C3'-endo (³ T ₂)	–	–	–	
				–	–	–	
[dGuo+H] ⁺	N7A	<i>anti</i>	1.508	C3'-endo (³ T ₂)	–	–	–
					–	–	–
	N7B	<i>anti</i>	1.501	C3'-exo (₃ T ⁴)	–	–	–
					–	–	–
O6A	<i>anti</i>	1.475	C2'-endo (² T ₃)	–	–	–	
				–	–	–	
N3A	<i>syn</i>	1.478	C4'-exo (₄ T ³)	∠N3H ⁺ ...O5'	160.4	1.853	
				–	–	–	

Geometric details based on structures optimized at the B3LYP/6-311+G(d,p) level of theory. Results for [Ado+H]⁺ and [dAdo+H]⁺ were taken from reference [67]. Results for [Guo+H]⁺ and [dGuo+H]⁺ were taken from reference [68].

N7B, the C2'-endo (²T₃) analogue of **N7A**, lies 1.4 kJ/mol above the ground-state conformation. **O6A** is the O6 protonated analogue of **N7B** with an *anti* nucleobase orientation and C2'-endo (²T₃) sugar pucker. The relative Gibbs energy of **O6A**, 33.9 kJ/mol above the ground-state conformation, results primarily from the differences in the proton affinities of these sites. Whereas the ground [Adofl+H]⁺ conformer is protonated at the N3 position, the **N3A** conformer of [Guofl+H]⁺ is 50.4 kJ/mol higher in B3LYP Gibbs energy than the ground-state conformation, **N7A**. **N3A** has a *syn* nucleobase orientation and C2'-endo (²T₁) sugar pucker. As with the [Adofl+H]⁺ conformers, the nucleobase orientations and sugar puckerings are stabilized by hydrogen bonds. The *anti* nucleobase orientations are preferentially stabilized by a non-canonical C8H...O5' hydrogen bond, whereas the *syn* nucleobase orientation of N3-protonated conformers possess an N3H⁺...O5' hydrogen bond. The sugar puckerings are preferentially stabilized by an O3'H...F hydrogen-bonding interaction.

Experimentally Populated [Adofl+H]⁺ Conformers

The experimental [Adofl+H]⁺ IRMPD action spectrum is compared with the predicted linear IR spectra for the **N3A**, **N3B**, **N1A**, and **N7A** conformers in Figure 6. Similar comparisons

for all unique calculated conformers are shown in Figure S6. Based on spectral comparisons, the conformers that were predominantly populated in the MS/MS experiments are **N3A** and **N1A**. Spectral comparisons indicate that **N3B** and **N7A** were not significantly populated in the MS/MS experiments.

The vibrations predicted for the **N3A** and **N1A** conformers nicely replicate all experimental absorption bands. However, calculated linear IR spectra often underestimate the intensities of the absorption bands in nonlinear IRMPD action spectra [103], as is particularly observed below ~1625 cm⁻¹ in the [Adofl+H]⁺ spectrum. The relative IRMPD yields of these vibrations are particularly amplified in the [Adofl+H]⁺ spectrum compared to those of [Ado+H]⁺ and [dAdo+H]⁺ (see Figure 4). Although **N1A** lies 23.6 kJ/mol higher in Gibbs energy than **N3A** in the gas-phase calculations, many of its spectral features match the experimental IRMPD spectrum exceptionally well. **N1A** lies only 4.9 kJ/mol higher in Gibbs energy than **N3A** in the PCM calculations with an implicit water solvent, suggesting some sampling of the solution-phase structures in the experimental measurements. Similar results were observed in the [Ado+H]⁺ and [dAdo+H]⁺ studies, where implicit solvation calculations were also found to lower the Gibbs energy difference between the **N3A** and **N1A** conformers to 2.4 and 4.5 kJ/mol, respectively, and both protonation sites were accessed in the experiments [67]. Some

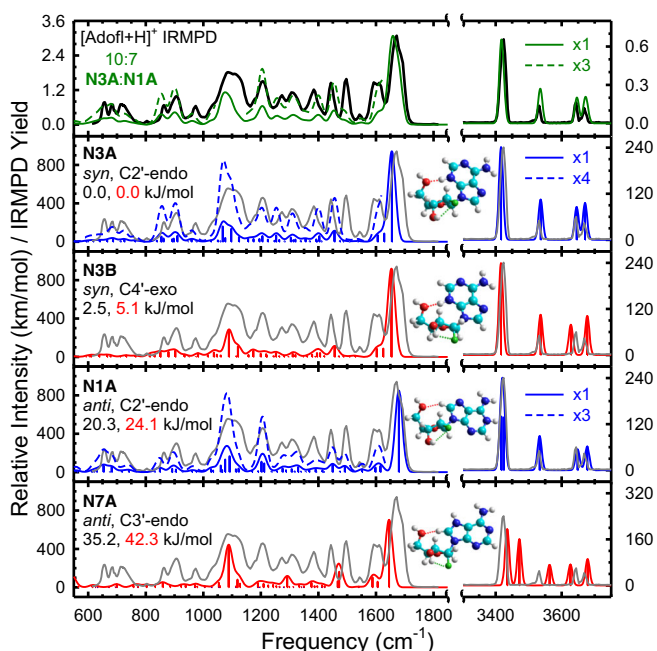


Figure 6. Comparisons of the experimental IRMPD action spectrum of [Adofl+H]⁺ (shown in black in the top panel and overlaid in gray and scaled to match the most intense feature in each region in all other panels) with theoretical linear IR spectra predicted for selected conformations of [Adofl+H]⁺ (shown in blue for experimentally populated conformers and in red for nonpopulated conformers in the bottom four panels). The optimized structure, conformer designation, nucleobase orientation, sugar puckering, and B3LYP/6-311+G(2d,2p) (shown in black) and MP2(full)/6-311+G(2d,2p) (shown in red) relative Gibbs energy at 298 K are given. The predicted IR spectrum for a 10:7 mixture of the **N3A** and **N1A** conformers, respectively, is overlaid in green in the top panel

[Adofl+H]⁺ experimental bands, especially at ~ 3420 , ~ 1600 , ~ 1550 , ~ 1500 , and ~ 1275 cm⁻¹, are more accurately replicated by **N1A** than by **N3A**. Other experimental bands, especially at ~ 3675 , ~ 1660 , ~ 1380 , and ~ 1100 cm⁻¹ are more accurately replicated by **N3A** than by **N1A**. A 10:7 combination of the **N3A** and **N1A** spectra, shown with a green line in the top plot, fits most of the experimental data well. This ratio reproduces the wide and angled shape of the feature at ~ 1625 – 1725 cm⁻¹.

The hydrogen-stretching region of the experimental [Adofl+H]⁺ spectrum (see the 3300–3750 cm⁻¹ region of Table 1 and Figure 6) has four distinct and highly informative absorption bands. The two highest frequency absorption bands at 3668 cm⁻¹ and 3644 cm⁻¹ correspond to the O5'-H and O3'-H stretches, respectively, of the **N3A** and **N1A** conformers. The O5'-H stretch of the **N3A** conformer matches the position of the observed experimental peak more accurately than that of the **N1A** conformer. The C2'-endo sugar puckering of **N3A** and **N1A** induce $\angle O3'H\cdots F$ hydrogen bond angles of $\sim 97.1^\circ$ and lengths of ~ 2.423 Å (see Table 4), resulting in red shifting of the O3'-H stretch away from the O5'-H stretch by 24 cm⁻¹ (see Table 1). The C4'-exo and C3'-endo sugar puckers of the **N3B** and **N7A**

conformers produce $\angle O3'H\cdots F$ hydrogen bond angles of $\sim 107.2^\circ$ and length of ~ 2.283 Å. The shorter and more on-axis O3'-H \cdots F interaction of **N3B** and **N7A** result in further red shifting of the O3'-H band to ~ 3625 cm⁻¹, where no appreciable resonant photon absorption is observed in the experimental IRMPD spectrum of [Adofl+H]⁺. The N-H stretches of **N3A**, **N3B**, and **N1A** all align well with the experimental spectrum. Further evidence for the exclusion of **N7A** from the experimental population is the mismatch of the predicted versus experimentally measured N-H vibrational frequencies in the region from ~ 3440 to ~ 3565 cm⁻¹.

The fingerprint region of the IRMPD spectrum of [Adofl+H]⁺ (see the 550–1850 cm⁻¹ region of Table 1 and Figure 6) displays an abundance of spectral features, all of which are replicated by the **N3A** and **N1A** conformers. The many features in the ~ 1150 – 1625 cm⁻¹ and ~ 600 – 1050 cm⁻¹ ranges are best replicated by the **N1A** conformer, whereas the more intense features at ~ 1625 – 1725 cm⁻¹ and 1050 – 1150 cm⁻¹ are better represented by the **N3A** conformer. The ~ 1625 – 1725 cm⁻¹ region is probably most diagnostic for the presence of both the **N3A** and **N1A** conformers to explain its distinct shape and width, with a slight ($\sim 10:7$) estimated preference for **N3A** over **N1A**. The **N3B** conformer displays parallel fingerprint absorptions to the **N3A** conformer, but with slight mismatching in the ~ 850 – 925 cm⁻¹ and ~ 1150 – 1225 cm⁻¹ regions and therefore could not be excluded from the experimental population based on the fingerprint region alone. The **N7A** conformer exhibits obvious spectral mismatches in the ~ 1425 – 1525 cm⁻¹ and ~ 1625 – 1725 cm⁻¹ regions.

Some conformers of [Adofl+H]⁺ not shown in Figure 6 have theoretical IR spectra that match the experimental IRMPD spectrum at least reasonably well (see Figure S6) and therefore cannot be conclusively excluded from the experimental population. However, the overall better quality match of the **N3A** and **N1A** predicted spectra with experiment over these conformers, as well as their higher Gibbs energies, suggest these additional conformers if present to be populated to a much lesser degree. These additional conformers with predicted spectra that reasonably match the experimental spectrum include **N3C**, **N3D**, **N3G**, **N1C**, **N1G**, **N1H**, and **N1I**. **N3C**, at 8.0 kJ/mol relative Gibbs energy, and **N3D**, at 13.9 kJ/mol, also have a *syn* nucleobase orientation, with **N3D** having a smaller $\angle O4'C1'N9C4$ dihedral angle. **N3C** has C4'-exo sugar puckering and does not contain an O3'-H \cdots F interaction, whereas **N3D** has C2'-endo sugar puckering and is stabilized by an O3'-H \cdots F interaction. **N3G**, at 29.8 kJ/mol, has a *syn* nucleobase orientation, C3'-endo sugar puckering, and an N3H⁺ \cdots O5' hydrogen bond. **N1C**, at 31.3 kJ/mol, has an *anti* nucleobase orientation, C3'-endo sugar puckering, and lacks an O3'-H \cdots F interaction. **N1G**, at 43.1 kJ/mol, has an *anti* nucleobase orientation and C3'-endo sugar puckering. **N1H**, at 44.3 kJ/mol, has an *anti* nucleobase orientation and C4'-exo sugar puckering. **N1I**, at 46.1 kJ/mol, has a *syn* nucleobase orientation and C4'-exo sugar puckering.

Experimentally Populated $[\text{Guofl}+\text{H}]^+$ Conformers

The experimental IRMPD action spectrum of $[\text{Guofl}+\text{H}]^+$ is compared with the predicted linear IR spectra for the **N7A**, **N7B**, **O6A**, and **N3A** conformers in Figure 7. Similar comparisons for all unique calculated conformers are shown in Figure S7. Based on spectral comparisons, the conformers that were predominantly populated in the MS/MS experiments are **N7A** and **N7B**. The data also suggest the **O6A** conformer may have been present in minor population. Spectral comparisons indicate that **N3A** was not populated in the MS/MS experiments.

The vibrations predicted for the **N7A**, **N7B**, and **O6A** conformers replicate all experimental absorption bands. Similar to that seen for $[\text{Adofl}+\text{H}]^+$, the predicted linear IR spectra for $[\text{Guofl}+\text{H}]^+$ generally underestimate absorption band intensities below $\sim 1625 \text{ cm}^{-1}$. The IRMPD yield for $[\text{Guofl}+\text{H}]^+$ in this region are higher than the parallel spectral features observed in the IRMPD spectra of $[\text{Guo}+\text{H}]^+$ and $[\text{dGuo}+\text{H}]^+$ (see Figure 5). The predicted IR spectrum of **N7A** matches the experimental spectrum better than **N7B** at ~ 675 , ~ 880 , ~ 950 , ~ 975 , and $\sim 1400 \text{ cm}^{-1}$, whereas the predicted spectrum for **N7B** matches the experimental spectrum better than **N7A** in the region from ~ 1050 – 1375 cm^{-1} .

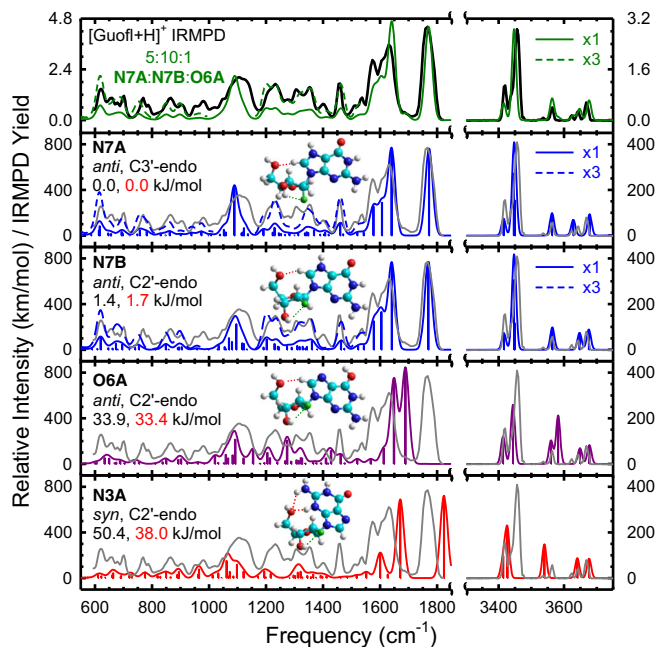


Figure 7. Comparisons of the experimental IRMPD action spectrum of $[\text{Guofl}+\text{H}]^+$ (shown in black in the top panel and overlaid in gray and scaled to match the most intense feature in each region in all other panels) with theoretical linear IR spectra predicted for selected conformations of $[\text{Guofl}+\text{H}]^+$ (shown in blue for the dominant experimentally populated conformers, in purple for minor experimentally populated conformers, and in red for nonpopulated conformers in the bottom four panels). The optimized structure, conformer designation, nucleobase orientation, sugar pucker, and B3LYP/6-311+G(2d,2p) (shown in black) and MP2(full)/6-311+G(2d,2p) (shown in red) relative Gibbs energy at 298 K are given. The predicted IR spectrum for a 5:10:1 mixture of the **N7A**, **N7B**, and **O6A** conformers, respectively, is overlaid in green in the top panel

A 5:10:1 linear combination of the **N7A**, **N7B**, and **O6A** spectra, respectively, fits most of the experimental data quite well (see Figure 7). Because the presence of **O6A** cannot be conclusively proven or ruled out based on the data, a linear combination of the predicted spectra for a 5:10 mixture of **N7A** and **N7B** is also compared with the experimental spectrum in Figure S8 for comparison. The fit degrades only very slightly when the **O6A** conformer is not included.

The hydrogen-stretching region of $[\text{Guofl}+\text{H}]^+$, the ~ 3300 – 3750 cm^{-1} region of Table 2 and Figure 7, displays seven distinct and highly informative resonant vibrational modes. The O5'-H stretch is the highest frequency vibration at 3668 cm^{-1} . The 5'-hydroxyl hydrogen atoms of most low-energy stable conformers do not participate in a canonical hydrogen-bonding interaction and therefore the IR spectra of most conformers reproduce this experimental band. The other two O-H stretches, at 3644 and 3624 cm^{-1} , arise from O3'-H stretches located in two distinct chemical environments. These two environments, readily replicated by **N7A** and **N7B**, are defined by the orientation and positioning of the O3'H \cdots F hydrogen-bonding interactions. The O3'H \cdots F geometry is primarily determined by the sugar pucker adopted by the conformer. **N7B**, with C2'-endo sugar pucker, has an $\angle\text{O3'H}\cdots\text{F}$ angle of 97.7° and O3'H \cdots F distance of 2.410 \AA and produces the O3'-H stretch at 3644 cm^{-1} . **N7A**, with C3'-endo sugar pucker, has an $\angle\text{O3'H}\cdots\text{F}$ angle of 106.1° and O3'H \cdots F distance of 2.310 \AA and produces the O3'-H stretch at 3624 cm^{-1} . The 3644 cm^{-1} band arising from **N7B** is more intense than the 3624 cm^{-1} band from **N7A**, suggesting that **N7B** is present in greater population than **N7A** in the experiments despite B3LYP predicting it to be 1.4 kJ/mol less stable in Gibbs energy. However, the shorter and more on-axis O3'H \cdots F interaction of **N7B** could potentially dampen the absorption of the O3'-H stretch and reduce the IRMPD yield in comparison to the longer and less on-axis O3'H \cdots F interaction of **N7A**; therefore, the suggested relative populations of the **N7A** and **N7B** conformers cannot be considered conclusive. The band at 3564 cm^{-1} arises from N2H₂ antisymmetric stretching. This vibrational mode is replicated by conformers with an unbound N2H₂ group, a feature of all conformers with an *anti* nucleobase orientation. **N7A**, **N7B**, and **O6A** all have *anti* nucleobase orientations and, therefore, all reproduce this absorption band, whereas **N3A**, with a *syn* nucleobase orientation in which the N2H₂ substituent engages in an O5' \cdots HN2 hydrogen-bonding interaction, does not. The smallest feature in the hydrogen-stretching region is found at 3536 cm^{-1} and is the most challenging band to explain. This band probably arises from the highly anharmonic O6-H⁺ stretch predicted at 3582 cm^{-1} for the most stable O6 protonated conformer, **O6A**. Red shifting of this type of O-H⁺ stretch has been previously observed in other IRMPD studies, particularly in the IRMPD spectra of $[\text{dCyd}+\text{H}]^+$, $[\text{Cyd}+\text{H}]^+$, and $[\text{Cydfl}+\text{H}]^+$ [9, 70]. However, the experimental O2-H⁺ stretch in these Cyd systems was red shifted from its predicted position by $\sim 20 \text{ cm}^{-1}$, whereas here the proposed assignment for the 3536 cm^{-1} peak corresponds to a red shift from theory

by an even larger difference of 46 cm^{-1} . However, the **O6A** conformer also readily replicates other necessary features of the $[\text{Guofl}+\text{H}]^+$ IRMPD spectrum, and therefore the interpretation of its minor presence seems justified. The most intense hydrogen stretch absorption occurs at 3456 cm^{-1} and primarily arises from a coalescence of N2H_2 symmetric and N7-H^+ stretches from the **N7A** and **N7B** conformers. The slight shoulder to the red of this peak is readily replicated by the N2H_2 symmetric stretch of **O6A**, as this band is predicted to be at a slightly lower vibrational frequency than the corresponding stretches of the **N7** protonated conformers. The lowest frequency peak in the hydrogen-stretching region is observed at 3420 cm^{-1} and corresponds to N1-H stretching. This vibrational mode is readily reproduced by most conformers independent of their specific structural motifs and is therefore generally undiagnostic.

The fingerprint region displays an abundance of spectral features. The highest intensity and largest vibrational frequency band observed at 1767 cm^{-1} corresponds to the C6=O carbonyl stretch of **N7** protonated conformers such as **N7A** and **N7B**. This band is not present in **O6** protonated conformations such as **O6A** due to shifting of the resonant vibrational frequency by the bonded proton. Although the C6=O carbonyl is not directly perturbed by protonation in the **N3** protonated conformers, the change in the chemical environment is sufficiently different to shift the predicted C6=O stretch to $\sim 1825\text{ cm}^{-1}$; this peak is not reproduced in the experimental spectrum, and therefore **N3** protonated conformers such as **N3A** are not populated in the experiments. The next major absorption band occurs at 1631 cm^{-1} and corresponds to the unbound N2H_2 scissoring primarily from the *anti* nucleobase orientation of the **N7A**, **N7B**, and **O6A** conformers. The *syn* orientation of **N3A** aids the formation of an $\text{N2H}\cdots\text{O5}'$ interaction that red shifts this vibration, adding further justification for elimination of **N3A** and other *syn* conformers from the experimental population. The shoulder to the blue of this peak arises from C5=C6 and C2=N3 stretching and O6-H^+ rocking of **O6A**.

Some conformers of $[\text{Guofl}+\text{H}]^+$ not shown in Figure 7 have predicted linear IR spectra that match the experimental IRMPD spectrum at least reasonably well (see Figure S7) and therefore cannot be conclusively excluded from the experimental population but are likely much less important than **N7A**, **N7B**, and **O6A**. These conformers include **N7C**, **N7E**, **N7F**, **N7H**, **N7I**, **O6B**, and **O6D**. **N7C**, at 6.3 kJ/mol , is structurally parallel to **N7A** and has an *anti* nucleobase orientation and $\text{C3}'\text{-endo}$ sugar puckering. **N7C** does not have an $\text{O3}'\text{H}\cdots\text{F}$ interaction, and thus no red shifting of its $\text{O3}'\text{-H}$ stretch is observed. **N7E**, at 19.6 kJ/mol , also has an *anti* nucleobase orientation and $\text{C3}'\text{-exo}$ sugar puckering, but has a wider $\angle\text{O4}'\text{C1}'\text{N9C4}$ dihedral angle than **N7C**. **N7F**, at 19.7 kJ/mol , has a *syn* nucleobase orientation and $\text{C2}'\text{-endo}$ sugar puckering stabilized by an $\text{O3}'\text{H}\cdots\text{F}$ interaction. **N7H**, at 29.7 kJ/mol , is parallel to **N7A**, except with a different $\text{O5}'$ orientation that disrupts the noncanonical $\text{C8H}\cdots\text{O5}'$ interaction. **N7I**, at 30.1 kJ/mol , has an *anti* nucleobase orientation and $\text{C1}'\text{-endo}$ sugar puckering. **O6B**, at 50.0 kJ/mol , has a *syn* nucleobase orientation and

$\text{C2}'\text{-endo}$ sugar puckering. **O6D**, at 89.6 kJ/mol , has an *anti* nucleobase orientation and $\text{C3}'\text{-exo}$ sugar puckering.

Effects of the 2'-Substituent on the Protonated Adenine and Guanine Nucleosides

Visual comparisons of selected comparable conformers of $[\text{Adofl}+\text{H}]^+$, $[\text{Ado}+\text{H}]^+$, and $[\text{dAdo}+\text{H}]^+$ are given in Figure S9 and of conformers of $[\text{Guofl}+\text{H}]^+$, $[\text{Guo}+\text{H}]^+$, and $[\text{dGuo}+\text{H}]^+$ in Figure S10. Comparisons of conformer energetics and structures are provided in Table 3 and Table 4. The purine $[\text{Nuofl}+\text{H}]^+$ conformers are highly parallel to their counterpart $[\text{Nuo}+\text{H}]^+$ and $[\text{dNuo}+\text{H}]^+$ conformers. The 2'- and 3'-hydroxy substituents of $[\text{Ado}+\text{H}]^+$ and $[\text{Guo}+\text{H}]^+$ allow for stabilization of a wider variety of hydrogen-bonding interactions in their sugar moieties than for $[\text{Adofl}+\text{H}]^+$ and $[\text{Guofl}+\text{H}]^+$. In $[\text{Adofl}+\text{H}]^+$, $[\text{Ado}+\text{H}]^+$, and $[\text{dAdo}+\text{H}]^+$, **N3** protonation is preferred over **N1** protonation by $\sim 22\text{ kJ/mol}$, which is favored over **N7** protonation by $\sim 13\text{ kJ/mol}$ or $\sim 35\text{ kJ/mol}$ relative to **N3** protonation. Implicit solvation lowers the Gibbs energies predicted for **N1** protonation of $[\text{Adofl}+\text{H}]^+$, $[\text{Ado}+\text{H}]^+$, and $[\text{dAdo}+\text{H}]^+$ to $\sim 5\text{ kJ/mol}$ above the corresponding ground-state conformation [67]. **N3** protonation preferentially favors the *syn* nucleobase orientation, whereas **N1** and **N7** protonation favor an *anti* nucleobase orientation. A slight $\sim 3\text{ kJ/mol}$ preference for $\text{C2}'\text{-endo}$ sugar puckering is computed for the **N3** and **N1** protonated conformers, whereas **N7** protonated conformers prefer $\text{C3}'\text{-endo}$ sugar puckering by $\sim 2\text{ kJ/mol}$. In $[\text{Guofl}+\text{H}]^+$, $[\text{Guo}+\text{H}]^+$, and $[\text{dGuo}+\text{H}]^+$, **N7** protonation is preferred over **O6** protonation by $\sim 36\text{ kJ/mol}$, and over **N3** protonation by $\sim 48\text{ kJ/mol}$. **N7** and **O6** protonation favor an *anti* nucleobase orientation, whereas **N3** protonation favors a *syn* nucleobase orientation. $\text{C3}'\text{-endo}$ sugar puckering is predicted to be preferred over $\text{C2}'\text{-endo}$ by $\sim 2\text{ kJ/mol}$ in **N7** protonated conformers, whereas **O6** protonation prefers $\text{C2}'\text{-endo}$ sugar puckering, and the **N3** protonated conformers do not exhibit a consistent trend.

The $\text{C1}'\text{-N9}$ glycosidic bond lengths decrease slightly from $[\text{dNuo}+\text{H}]^+$ to $[\text{Nuo}+\text{H}]^+$ to $[\text{Nuofl}+\text{H}]^+$ for the purine nucleosides. The $\text{C1}'\text{-N9}$ glycosidic bond lengths decrease by $\sim 0.008\text{ \AA}$ from $[\text{dAdo}+\text{H}]^+$ to $[\text{Ado}+\text{H}]^+$ and by $\sim 0.001\text{ \AA}$ from $[\text{Ado}+\text{H}]^+$ to $[\text{Adofl}+\text{H}]^+$. Similarly, the $\text{C1}'\text{-N9}$ bond lengths shrink by $\sim 0.013\text{ \AA}$ from $[\text{dGuo}+\text{H}]^+$ to $[\text{Guo}+\text{H}]^+$ and by $\sim 0.001\text{ \AA}$ from $[\text{Guo}+\text{H}]^+$ to $[\text{Guofl}+\text{H}]^+$. These trends are conceptually consistent with the ER-CID survival yield results that suggest increasing glycosidic bond stability from $[\text{dNuo}+\text{H}]^+$ to $[\text{Nuo}+\text{H}]^+$ to $[\text{Nuofl}+\text{H}]^+$. However, the experimental survival yields show a larger increase in $\text{CID}_{50\%}$ from $[\text{Nuo}+\text{H}]^+$ to $[\text{Nuofl}+\text{H}]^+$ than is suggested by the calculated glycosidic bond lengths alone. Parallel trends were observed in the pyrimidine $[\text{Nuofl}+\text{H}]^+$, $[\text{Nuo}+\text{H}]^+$, and $[\text{dNuo}+\text{H}]^+$ survival yield analyses and $\text{C1}'\text{-N1}$ glycosidic bond lengths [9].

Shorter and more linear, i.e., nearer to 180° , interactions are indicative of stronger hydrogen bonds [33, 35, 104–106]. In nucleoside sugar rings, sugar puckering dictates the geometry, and thus the relative strength, of their intramolecular hydrogen

bonds. Purine [Nuofl+H]⁺ conformers with C2'-endo character have ∠O3'H⋯F angles of ~97.5° and lengths of ~2.416 Å, whereas conformers with C3'-endo or C4'-exo puckers have ∠O3'H⋯F angles of ~106.8° and lengths of ~2.292 Å (see Table 4). Red shifting in both the purine [Nuofl+H]⁺ O3'-H stretches occur due to these hydrogen-bonding interactions with fluorine. The longer and less direct O3'H⋯F interactions of C2'-endo conformers red shift the O3'-H stretches ~24 cm⁻¹ away from the O5'-H stretches, whereas the shorter and more direct O3'H⋯F interactions of C3'-endo and C4'-exo conformers red shift the O3'-H stretches ~44 cm⁻¹ away from the O5'-H stretches. Parallel intramolecular OH⋯O hydrogen-bonding interactions are observed in the sugar moiety of the experimentally populated [Nuo+H]⁺ conformers [54, 67]. Conformers with O2'H⋯O interactions were generally calculated as lower in Gibbs energy than conformers with O3'H⋯O interactions. These O2'H⋯O interactions have angles of ~114.5° and lengths of ~2.123 Å regardless of their sugar puckering (see Table 4). Therefore, these [Nuo+H]⁺ OH⋯O hydrogen bonds are shorter and more linear than those of the [Nuofl+H]⁺ OH⋯F hydrogen bonds and thus provide greater stabilization. These calculations are consistent with condensed phase studies, which have generally demonstrated OH⋯O interactions to be shorter and more stable than parallel OH⋯F interactions [32–35, 38]. Regardless, no O2'-H stretch red shifting dependence on the sugar puckering or ∠OH⋯O angle is observed in the experimental and predicted [Nuo+H]⁺ IRMPD spectra [54, 67]. Parallel observations were found for the pyrimidine nucleosides, where geometric variations in the O3'H⋯F interactions red shift the O3'-H stretches to different degrees, whereas OH⋯O interactions display no such variation [9, 69–71]. Thus, the red shifting of the O3'-H stretches observed in the [Nuofl+H]⁺ spectra must result both from the strength of the hydrogen bonds and the highly electronegative character of fluorine.

Conclusions

The structural and energetic effects of 2'-fluoro modification on the purine nucleosides were investigated using IRMPD action spectroscopy, ER-CID with survival yield analysis, and electronic structure calculations. Results for the [Adofl+H]⁺ and [Guofl+H]⁺ are reported here and compared with previous work on their counterpart canonical purine systems [Ado+H]⁺, [Guo+H]⁺, [dAdo+H]⁺, and [dGuo+H]⁺ [67, 68], as well as with [Cydfl+H]⁺ and [Urdfl+H]⁺ [9]. Unimolecular dissociation of [Adofl+H]⁺ and [Guofl+H]⁺ via IRMPD and CID activation results in cleavage of their C1'-N9 glycosidic bonds with retention of the excess proton by the nucleobase; no other fragmentation pathways were observed. Based on survival yield analysis of the ER-CID experiments, 2'-fluoro modification of the protonated DNA and RNA purine nucleosides strengthens their C1'-N9 glycosidic bonds. These experimental results are reinforced by the shrinking of the C1'-N9 glycosidic bonds predicted across the [dNuo+H]⁺, [Nuo+H]⁺, and

[Nuofl+H]⁺ series. This behavior can be further explained based on increasing destabilization of the proposed oxocarbenium ion intermediates [53, 54] with increasing electronegativity of the 2'-substituent: H < OH < F. In general, the absorption band identities and resonant vibrational frequencies of the experimental IRMPD spectra of [Adofl+H]⁺ and [Guofl+H]⁺ are parallel to their analogous DNA and RNA forms. However, important differences are also apparent. The [Nuofl+H]⁺ systems have higher IR absorption efficiency, resulting in greater IRMPD yields compared with the [Nuo+H]⁺ and [dNuo+H]⁺ systems. Additionally, the relative peak intensities in most of the fingerprint region are much greater for [Nuofl+H]⁺ than [Nuo+H]⁺ and [dNuo+H]⁺. Evidence for intramolecular gas-phase O3'H⋯F hydrogen bonds is found in the hydrogen-stretching region of the IRMPD spectra of [Adofl+H]⁺ and [Guofl+H]⁺ and allows for reliable sugar puckering determinations, which are not possible for the canonical analogues. Recent studies on the pyrimidine [Nuofl+H]⁺ also displayed clear spectroscopic evidence for gas-phase O3'H⋯F interactions [9]. For [Adofl+H]⁺, the **N3A** and **N1A** conformers are populated experimentally, with a slight preference for **N3A** over **N1A** suggested by the spectral comparisons. **N3A**, the ground-state conformation, has a *syn* nucleobase orientation and C2'-endo sugar puckering, whereas **N1A**, at 20.3 kJ/mol, has an *anti* nucleobase orientation and C2'-endo sugar puckering. C3'-endo and C4'-exo sugar puckerings, such as in **N3B** and **N1B**, were not present in the experimental population. For [Guofl+H]⁺, the **N7A** and **N7B** conformers are dominant in the experimental population with a slight preference for **N7B**. **O6A** is also suggested to be a minor contributor to the experimental population. **N7A**, the ground-state conformation, has an *anti* nucleobase orientation and C3'-endo sugar puckering, whereas **N7B**, at 1.4 kJ/mol, has *anti* nucleobase orientation and C2'-endo sugar puckering. **O6A**, at 33.9 kJ/mol, has an *anti* nucleobase orientation and C2'-endo sugar puckering. Overall, 2'-fluoro modifications to the canonical DNA and RNA purine nucleosides impart minimal structural changes and result in overall highly parallel conformers among the analogous [Nuofl+H]⁺, [Nuo+H]⁺, and [dNuo+H]⁺ systems [67, 68]. In contrast, substantial electronic effects are produced by the highly electronegative 2'-fluoro modification and are readily apparent in the IRMPD, ER-CID, and theoretical results.

Acknowledgements

This work was supported by the National Science Foundation grant numbers OISE-0730072 and OISE-1357887 for international travel and IRMPD experiments, DBI-0922819 for the Bruker amaZon ETD QIT MS, and CHE-1709789 for all other research costs. The authors gratefully acknowledge the Nederlandse Organisatie voor Wetenschappelijk Onderzoek (NWO) for the support of the FELIX Laboratory. Z.J.D., C.C.H., Y.Z., and L.A.H. gratefully acknowledge the support from WSU Thomas C. Rumble Graduate Fellowships. Z.J.D. is thankful for the additional support from the WSU Joseph

Jasper Scholarship for Graduate Students in Chemistry. The authors are very grateful for WSU C&IT for the computer time and support. The authors are exceedingly grateful for the skillful assistance of the FELIX Laboratory staff.

References

- Voet, D., Voet, J.G., Pratt, C.W.: *Fundamentals of biochemistry: life at the molecular level*, 2nd edn. John Wiley & Sons, Inc., Hoboken, NJ (2006)
- Chatterjee, N., Walker, G.C.: Mechanisms of DNA damage, repair, and mutagenesis. *Environ. Mol. Mutagen.* **58**, 235–263 (2017)
- Antoniali, G., Malfatti, M.C., Tell, G.: Unveiling the non-repair face of the base excision repair pathway in RNA processing: a missing link between DNA repair and gene expression? *DNA Repair.* **56**, 65–74 (2017)
- Vohhodina, J., Harkin, D.P., Savage, K.I.: Dual roles of DNA repair enzymes in RNA biology/post-transcriptional control. *Wiley Interdiscip. Rev. RNA.* **7**, 604–619 (2016)
- Wallace, S.S.: Base excision repair: a critical player in many games. *DNA Repair.* **19**, 14–26 (2014)
- Tsutakawa, S.E., Lafrance-Vanasse, J., Tainer, J.A.: The cutting edges in DNA repair, licensing, and fidelity: DNA and RNA repair nucleases sculpt DNA to measure twice, cut once. *DNA Repair.* **19**, 95–107 (2014)
- Drohat, A.C., Maiti, A.: Mechanisms for enzymatic cleavage of the N-glycosidic bond in DNA. *Org. Biomol. Chem.* **12**, 8367–8378 (2014)
- Bennett, M.T., Rodgers, M.T., Hebert, A.S., Ruslander, L.E., Eisele, L., Drohat, A.C.: Specificity of human thymine DNA glycosylase depends on N-glycosidic bond stability. *J. Am. Chem. Soc.* **128**, 12510–12519 (2006)
- Devereaux, Z.J., Roy, H.A., He, C.C., Zhu, Y., Cunningham, N.A., Hamlow, L.A., Berden, G., Oomens, J., Rodgers, M.T.: Influence of 2'-fluoro modification on glycosidic bond stabilities and gas-phase ion structures of protonated pyrimidine nucleosides. *J. Fluorine Chem.* **219**, 10–22 (2019)
- Gillis, E.P., Eastman, K.J., Hill, M.D., Donnelly, D.J., Meanwell, N.A.: Applications of fluorine in medicinal chemistry. *J. Med. Chem.* **58**, 8315–8359 (2015)
- Liu, P., Sharon, A., Chu, C.K.: Fluorinated nucleosides: synthesis and biological implication. *J. Fluorine Chem.* **129**, 743–766 (2008)
- Hagmann, W.K.: The many roles for fluorine in medicinal chemistry. *J. Med. Chem.* **51**, 4359–4369 (2008)
- Isanbor, C., O'Hagan, D.: Fluorine in medicinal chemistry: a review of anti-cancer agents. *J. Fluorine Chem.* **127**, 303–319 (2006)
- Bégué, J.-P., Bonnet-Delpon, D.: Recent advances (1995–2005) in fluorinated pharmaceuticals based on natural products. *J. Fluorine Chem.* **127**, 992–1012 (2006)
- Böhm, H.J., Banner, D., Bendels, S., Kansy, M., Kuhn, B., Müller, K., Obst-Sander, U., Stahl, M.: Fluorine in medicinal chemistry. *ChemBioChem.* **5**, 637–643 (2004)
- Ismail, F.M.: Important fluorinated drugs in experimental and clinical use. *J. Fluorine Chem.* **118**, 27–33 (2002)
- Pankiewicz, K.W., Krzeminski, J., Ciszewski, L.A., Ren, W.Y., Watanabe, K.A.: A synthesis of 9-(2-deoxy-2-fluoro- β -D-arabinofuranosyl) adenine and hypoxanthine. An effect of C3'-endo to C2'-endo conformational shift on the reaction course of 2'-hydroxyl group with DAST. *J. Org. Chem.* **57**, 553–559 (1992)
- Codington, J.F., Doerr, L.L., Fox, J.J.: Nucleosides. XVIII. Synthesis of 2'-fluorothymidine, 2'-fluorodeoxyuridine, and other 2'-halogeno-2'-deoxy nucleosides. *J. Org. Chem.* **29**, 558–564 (1964)
- Pankiewicz, K.W.: Fluorinated nucleosides. *Carbohydr. Res.* **327**, 87–105 (2000)
- Qiu, X.-L., Xu, X.-H., Qing, F.-L.: Recent advances in the synthesis of fluorinated nucleosides. *Tetrahedron.* **4**, 789–843 (2010)
- Wójtowicz-Rajchel, H.: Synthesis and applications of fluorinated nucleoside analogues. *J. Fluorine Chem.* **143**, 11–48 (2012)
- Ranganathan, R.: Modification of the 2'-position of purine nucleosides: syntheses of 2'- α -substituted-2'-deoxyadenosine analogs. *Tetrahedron Lett.* **15**, 1291–1294 (1977)
- Pauling, L.: *The nature of the chemical bond and the structure of molecules and crystals: An introduction to modern structural chemistry.* Cornell University Press, Ithaca (1960)
- O'Hagan, D.: Understanding organofluorine chemistry. An introduction to the C-F bond. *Chem. Soc. Rev.* **37**, 308–319 (2008)
- Smart, B.E.: Fluorine substituent effects (on bioactivity). *J. Fluorine Chem.* **109**, 3–11 (2001)
- Bondi, A.: Van der Waals volumes and radii. *J. Phys. Chem.* **68**, 441–451 (1964)
- Purser, S., Moore, P.R., Swallow, S., Gouverneur, V.: Fluorine in medicinal chemistry. *Chem. Soc. Rev.* **37**, 320–330 (2008)
- Huang, P., Chubb, S., Hertel, L.W., Grindey, G.B., Plunkett, W.: Action of 2',2'-difluorodeoxycytidine on DNA synthesis. *Cancer Res.* **51**, 6110–6117 (1991)
- Grem, J.L.: 5-Fluorouracil: forty-plus and still ticking. A review of its preclinical and clinical development. *Investig. New Drugs.* **18**, 299–313 (2000)
- Ewald, B., Sampath, D., Plunkett, W.: Nucleoside analogs: molecular mechanisms signaling cell death. *Oncogene.* **27**, 6522–6537 (2008)
- Shugrue, C., DeFrancisco, J., Metrano, A., Brink, B., Nomoto, R., Linton, B.: Detection of weak hydrogen bonding to fluoro and nitro groups in solution using H/D exchange. *Org. Biomol. Chem.* **14**, 2223–2227 (2016)
- Shimoni, L., Glusker, J.P.: The geometry of intermolecular interactions in some crystalline fluorine-containing organic compounds. *Struct. Chem.* **5**, 383–397 (2015)
- Champagne, P.A., Desroches, J., Paquin, J.-F.: Organic fluorine as a hydrogen-bond acceptor: recent examples and applications. *Synthesis.* **47**, 306–322 (2015)
- Dalvit, C., Invernizzi, C., Vulpetti, A.: Fluorine as a hydrogen-bond acceptor: experimental evidence and computational calculations. *Chem. Eur. J.* **20**, 11058–11068 (2014)
- Schneider, H.-J.: Hydrogen bonds with fluorine. Studies in solution, in gas phase and by computations, conflicting conclusions from crystallographic analyses. *Chem. Sci.* **3**, 1381–1394 (2012)
- Brammer, L., Bruton, E.A., Sherwood, P.: Understanding the behavior of halogens as hydrogen bond acceptors. *Cryst. Growth Des.* **1**, 277–290 (2001)
- Dunitz, J.D., Taylor, R.: Organic fluorine hardly ever accepts hydrogen bonds. *Chem. Eur. J.* **3**, 89–98 (1997)
- Howard, J.A.K., Hoy, V.J., O'Hagan, D., Smith, G.T.: How good is fluorine as a hydrogen bond acceptor? *Tetrahedron.* **52**, 12613–12622 (1996)
- Zhu, Y., Hamlow, L.A., He, C.C., Lee, J.K., Gao, J., Berden, G., Oomens, J., Rodgers, M.T.: Gas-phase conformations and N-glycosidic bond stabilities of sodium cationized 2'-deoxyguanosine and guanosine: sodium cations preferentially bind to the guanine residue. *J. Phys. Chem. B.* **121**, 4048–4060 (2017)
- Zhu, Y., Hamlow, L.A., He, C.C., Strobehn, S.F., Lee, J.K., Gao, J., Berden, G., Oomens, J., Rodgers, M.T.: Influence of sodium cationization versus protonation on the gas-phase conformations and glycosidic bond stabilities of 2'-deoxyadenosine and adenosine. *J. Phys. Chem. B.* **120**, 8892–8904 (2016)
- Zhu, Y., Roy, H.A., Cunningham, N.A., Strobehn, S.F., Gao, J., Munshi, M.U., Berden, G., Oomens, J., Rodgers, M.T.: IRMPD action spectroscopy, ER-CID experiments, and theoretical studies of sodium cationized thymidine and 5-methyluridine: kinetic trapping during the ESI desolvation process preserves the solution structure of [Thd+Na]⁺. *J. Am. Soc. Mass Spectrom.* **28**, 2423–2437 (2017)
- Zhu, Y., Roy, H.A., Cunningham, N.A., Strobehn, S.F., Gao, J., Munshi, M.U., Berden, G., Oomens, J., Rodgers, M.T.: Effects of sodium cationization versus protonation on the conformations and N-glycosidic bond stabilities of sodium cationized Urd and dUrd: solution conformation of [Urd+Na]⁺ is preserved upon ESI. *Phys. Chem. Chem. Phys.* **19**, 17637–17652 (2017)
- Zhu, Y., Hamlow, L.A., He, C.C., Roy, H.A., Cunningham, N.A., Munshi, M., Berden, G., Oomens, J., Rodgers, M.T.: Conformations and N-glycosidic bond stabilities of sodium cationized 2'-deoxycytidine and cytidine: solution conformation of [Cyd+Na]⁺ is preserved upon ESI. *Int. J. Mass Spectrom.* **429**, 18–27 (2017)
- He, C.C., Hamlow, L.A., Devereaux, Z.J., Zhu, Y., Nei, Y.-w., Fan, L., McNary, C.P., Maitre, P., Steinmetz, V., Schindler, B., Compagnon, I., Armentrout, P.B., Rodgers, M.T.: Structural and energetic effects of 2'-ribose methylation of protonated purine nucleosides. *J. Phys. Chem. B.* **122**, 9147–9160 (2018)

45. Devereaux, Z.J., Zhu, Y., Rodgers, M.T.: Relative glycosidic bond stabilities of naturally-occurring methylguanosines: 7-methylation is intrinsically activating. *Eur. J. Mass Spectrom.* **25**, 16–29 (2019)
46. Yang, B., Rodgers, M.T.: Base-pairing energies of protonated nucleoside base pairs of dCyd and m⁵dCyd: implications for the stability of DNA i-motif conformations. *J. Am. Soc. Mass Spectrom.* **26**, 1394–1403 (2015)
47. Yang, B., Wu, R.R., Rodgers, M.T.: Base-pairing energies of proton-bound dimers and proton affinities of 1-methyl-5-halocytosines: implications for the effects of halogenation on the stability of the DNA i-motif. *J. Am. Soc. Mass Spectrom.* **26**, 1469–1482 (2015)
48. Yang, B., Moehlig, A.R., Frieler, C.E., Rodgers, M.T.: Base-pairing energies of protonated nucleobase pairs and proton affinities of 1-methylated cytosines: model systems for the effects of the sugar moiety on the stability of DNA i-motif conformations. *J. Phys. Chem. B.* **119**, 1857–1868 (2015)
49. Yang, B., Rodgers, M.T.: Base-pairing energies of proton-bound heterodimers of cytosine and modified cytosines: implications for the stability of DNA i-motif conformations. *J. Am. Chem. Soc.* **136**, 282–290 (2014)
50. Yang, B., Wu, R.R., Rodgers, M.T.: Base-pairing energies of proton-bound homodimers determined by guided ion beam tandem mass spectrometry: application to cytosine and 5-substituted cytosines. *Anal. Chem.* **85**, 11000–11006 (2013)
51. Yang, Z., Rodgers, M.T.: Influence of methylation on the properties of uracil and its noncovalent interactions with alkali metal ions: threshold collision-induced dissociation and theoretical studies. *Int. J. Mass Spectrom.* **241**, 225–242 (2005)
52. Yang, Z., Rodgers, M.T.: Influence of halogenation on the properties of uracil and its noncovalent interactions with alkali metal ions. Threshold collision-induced dissociation and theoretical studies. *J. Am. Chem. Soc.* **126**, 16217–16226 (2004)
53. Wu, R.R., Rodgers, M.T.: Mechanisms and energetics for N-glycosidic bond cleavage of protonated adenine nucleosides: N3 protonation induces base rotation and enhances N-glycosidic bond stability. *Phys. Chem. Chem. Phys.* **18**, 16021–16032 (2016)
54. Wu, R.R., Chen, Y., Rodgers, M.T.: Mechanisms and energetics for N-glycosidic bond cleavage of protonated 2'-deoxyguanosine and guanosine. *Phys. Chem. Chem. Phys.* **18**, 2968–2980 (2016)
55. Wu, R.R., Rodgers, M.T.: O2 protonation controls threshold behavior for N-glycosidic bond cleavage of protonated cytosine nucleosides. *J. Phys. Chem. B.* **120**, 4803–4811 (2016)
56. Wu, R.R., Rodgers, M.T.: Tautomerization lowers the activation barriers for N-glycosidic bond cleavage of protonated uridine and 2'-deoxyuridine. *Phys. Chem. Chem. Phys.* **18**, 24451–24459 (2016)
57. Yang, B., Wu, R.R., Berden, G., Oomens, J., Rodgers, M.T.: Infrared multiple photon dissociation action spectroscopy of proton-bound dimers of cytosine and modified cytosines: effects of modifications on gas-phase conformations. *J. Phys. Chem. B.* **117**, 14191–14201 (2013)
58. Ung, H.U., Moehlig, A.R., Kudla, R.A., Mueller, L.J., Oomens, J., Berden, G., Morton, T.H.: Proton-bound dimers of 1-methylcytosine and its derivatives: vibrational and NMR spectroscopy. *Phys. Chem. Chem. Phys.* **15**, 19001–19012 (2013)
59. Oomens, J., Moehlig, A.R., Morton, T.H.: Infrared multiple photon dissociation (IRMPD) spectroscopy of the proton-bound dimer of 1-methylcytosine in the gas phase. *J. Phys. Chem. Lett.* **1**, 2891–2897 (2010)
60. Crampton, K.T., Rathur, A.I., Nei, Y.-w., Berden, G., Oomens, J., Rodgers, M.T.: Protonation preferentially stabilizes minor tautomers of the halouracils: IRMPD action spectroscopy and theoretical studies. *J. Am. Soc. Mass Spectrom.* **23**, 1469–1478 (2012)
61. Nei, Y.-w., Akinyemi, T.E., Kaczan, C.M., Steill, J.D., Berden, G., Oomens, J., Rodgers, M.T.: Infrared multiple photon dissociation action spectroscopy of sodiated uracil and thiouracils: effects of thio-keto-substitution on gas-phase conformation. *Int. J. Mass Spectrom.* **308**, 191–202 (2011)
62. Rajabi, K., Gillis, E.A., Fridgen, T.D.: Structures of alkali metal ion-adenine complexes and hydrated complexes by IRMPD spectroscopy and electronic structure calculations. *J. Phys. Chem. A.* **114**, 3449–3456 (2010)
63. Nei, Y.-w., Akinyemi, T.E., Steill, J.D., Oomens, J., Rodgers, M.T.: Infrared multiple photon dissociation action spectroscopy of protonated uracil and thiouracils: effects of thio-keto-substitution on gas-phase conformation. *Int. J. Mass Spectrom.* **297**, 139–151 (2010)
64. Salpin, J.-Y., Haldys, V., Steinmetz, V., Léon, E., Yáñez, M., Montero-Campillo, M.M.: Protonation of methyluracils in the gas phase: the particular case of 3-methyluracil. *Int. J. Mass Spectrom.* **429**, 47–55 (2018)
65. Kaczan, C.M., Rathur, A.I., Wu, R.R., Chen, Y., Austin, C.A., Berden, G., Oomens, J., Rodgers, M.T.: Infrared multiple photon dissociation action spectroscopy of sodium cationized halouracils: effects of sodium cationization and halogenation on gas-phase conformation. *Int. J. Mass Spectrom.* **378**, 76–85 (2015)
66. Salpin, J.-Y., Guillaumont, S., Tortajada, J., MacAleese, L., Lemaire, J., Maitre, P.: Infrared spectra of protonated uracil, thymine and cytosine. *ChemPhysChem.* **8**, 2235–2244 (2007)
67. Wu, R.R., Yang, B., Berden, G., Oomens, J., Rodgers, M.T.: Gas-phase conformations and energetics of protonated 2'-deoxyadenosine and adenosine: IRMPD action spectroscopy and theoretical studies. *J. Phys. Chem. B.* **119**, 2795–2805 (2015)
68. Wu, R.R., Yang, B., Berden, G., Oomens, J., Rodgers, M.T.: Gas-phase conformations and energetics of protonated 2'-deoxyguanosine and guanosine: IRMPD action spectroscopy and theoretical studies. *J. Phys. Chem. B.* **118**, 14774–14784 (2014)
69. Wu, R.R., Yang, B., Frieler, C.E., Berden, G., Oomens, J., Rodgers, M.T.: 2,4-Dihydroxy and O2 protonated tautomers of dThd and Thd coexist in the gas phase: methylation alters protonation preferences versus dUrd and Urd. *J. Am. Soc. Mass Spectrom.* **27**, 410–421 (2016)
70. Wu, R.R., Yang, B., Frieler, C.E., Berden, G., Oomens, J., Rodgers, M.T.: N3 and O2 protonated tautomeric conformations of 2'-deoxycytidine and cytidine coexist in the gas phase. *J. Phys. Chem. B.* **119**, 5773–5784 (2015)
71. Wu, R.R., Yang, B., Frieler, C.E., Berden, G., Oomens, J., Rodgers, M.T.: Diverse mixtures of 2,4-dihydroxy tautomers and O4 protonated conformers of uridine and 2'-deoxyuridine coexist in the gas phase. *Phys. Chem. Chem. Phys.* **17**, 25978–25988 (2015)
72. Salpin, J.-Y., Scuderi, D.: Structure of protonated thymidine characterized by infrared multiple photon dissociation and quantum calculations. *Rapid Commun. Mass Spectrom.* **29**, 1898–1904 (2015)
73. Filippi, A., Frascchetti, C., Rondino, F., Piccirillo, S., Steinmetz, V., Guidoni, L., Speranza, M.: Protonated pyrimidine nucleosides probed by IRMPD spectroscopy. *Int. J. Mass Spectrom.* **354**(355), 54–61 (2013)
74. Hamlow, L.A., Zhu, Y., Devereaux, Z.J., Cunningham, N.A., Berden, G., Oomens, J., Rodgers, M.T.: Modified quadrupole ion trap mass spectrometer for infrared ion spectroscopy: application to protonated thiated uridines. *J. Am. Soc. Mass Spectrom.* **29**, 2125–2137 (2018)
75. Salpin, J.-Y., Guillaumont, S., Ortiz, D., Tortajada, J., Maitre, P.: Direct evidence for tautomerization of the uracil moiety within the Pb²⁺/uridine-5'-monophosphate complex: a combined tandem mass spectrometry and IRMPD study. *Inorg. Chem.* **50**, 7769–7778 (2011)
76. Wu, R.R., He, C.C., Hamlow, L.A., Nei, Y.W., Berden, G., Oomens, J., Rodgers, M.T.: Protonation induces base rotation of purine nucleotides pdGuo and pGuo. *Phys. Chem. Chem. Phys.* **18**, 15081–15090 (2016)
77. Wu, R.R., He, C.C., Hamlow, L.A., Nei, Y.-w., Berden, G., Oomens, J., Rodgers, M.T.: N3 protonation induces base rotation of 2'-deoxyadenosine-5'-monophosphate and adenosine-5'-monophosphate. *J. Phys. Chem. B.* **120**, 4616–4624 (2016)
78. Wu, R.R., Hamlow, L.A., He, C.C., Nei, Y.W., Berden, G., Oomens, J., Rodgers, M.T.: The intrinsic basicity of the phosphate backbone exceeds that of uracil and thymine residues: protonation of the phosphate moiety is preferred over the nucleobase for pdThd and pUrd. *Phys. Chem. Chem. Phys.* **19**, 30351–30361 (2017)
79. Wu, R.R., Hamlow, L.A., He, C.C., Nei, Y.-w., Berden, G., Oomens, J., Rodgers, M.T.: N3 and O2 protonated conformers of the cytosine mononucleotides coexist in the gas phase. *J. Am. Soc. Mass Spectrom.* **28**, 1638–1646 (2017)
80. Salpin, J.-Y., Gamiotte, L., Tortajada, J., Besson, T., Maitre, P.: Structure of Pb²⁺/dCMP and Pb²⁺/CMP complexes as characterized by tandem mass spectrometry and IRMPD spectroscopy. *Int. J. Mass Spectrom.* **304**, 154–164 (2011)
81. Valle, J.J., Eyler, J.R., Oomens, J., Moore, D.T., van der Meer, A., von Helden, G., Meijer, G., Hendrickson, C.L., Marshall, A.G., Blakney, G.T.: Free electron laser-Fourier transform ion cyclotron resonance mass spectrometry facility for obtaining infrared multiphoton dissociation spectra of gaseous ions. *Rev. Sci. Instrum.* **76**, 023103–023107 (2005)
82. Oepts, D., van der Meer, A., van Amersfoort, P.: The free-electron-laser user facility FELIX. *Infrared Phys. Technol.* **36**, 297–308 (1995)
83. Martens, J., Berden, G., Gebhardt, C.R., Oomens, J.: Infrared ion spectroscopy in a modified quadrupole ion trap mass spectrometer at the

- FELIX free electron laser laboratory. *Rev. Sci. Instrum.* **87**, 103108 (2016)
84. Frisch, M.J., Trucks, G.W., Schlegel, H.B., Scuseria, G.E., Robb, M.A., et al.: *Gaussian 09*. Gaussian Inc., Wallingford, CT (2009)
85. Merrick, J.P., Moran, D., Radom, L.: An evaluation of harmonic vibrational frequency scale factors. *J. Phys. Chem. A*. **111**, 11683–11700 (2007)
86. Egli, M., Saenger, W.: *Principles of nucleic acid structure*, pp. 16–104. Springer Science & Business Media, New York (1984)
87. Altona, C., Sundaralingam, M.: Conformational analysis of the sugar ring in nucleosides and nucleotides. Improved method for the interpretation of proton magnetic resonance coupling constants. *J. Am. Chem. Soc.* **95**, 2333–2344 (1973)
88. Altona, C., Sundaralingam, M.: Conformational analysis of the sugar ring in nucleosides and nucleotides. New description using the concept of pseudorotation. *J. Am. Chem. Soc.* **94**, 8205–8212 (1972)
89. Polfer, N.C.: Infrared multiple photon dissociation spectroscopy of trapped ions. *Chem. Soc. Rev.* **40**, 2211–2221 (2011)
90. Polfer, N.C., Oomens, J.: Vibrational spectroscopy of bare and solvated ionic complexes of biological relevance. *Mass Spectrom. Rev.* **28**, 468–494 (2009)
91. McLuckey, S.A.: Principles of collisional activation in analytical mass spectrometry. *J. Am. Soc. Mass Spectrom.* **3**, 599–614 (1992)
92. Hart, K.J., McLuckey, S.A.: Relative dissociation energy measurements using ion trap collisional activation. *J. Am. Soc. Mass Spectrom.* **5**, 250–259 (1994)
93. Memboeuf, A., Jullien, L., Lartia, R., Brasme, B., Gimbert, Y.: Tandem mass spectrometric analysis of a mixture of isobars using the survival yield technique. *J. Am. Soc. Mass Spectrom.* **22**, 1744–1752 (2011)
94. Memboeuf, A., Nasioudis, A., Indelicato, S., Pollreisz, F., Kuki, A., Kéki, S., van den Brink, O.F., Vékey, K.R., Drahos, L.: Size effect on fragmentation in tandem mass spectrometry. *Anal. Chem.* **82**, 2294–2302 (2010)
95. Kuki, Á., Nagy, L., Memboeuf, A., Drahos, L., Vékey, K., Zsuga, M., Kéki, S.: Energy-dependent collision-induced dissociation of lithiated polytetrahydrofuran: effect of the size on the fragmentation properties. *J. Am. Soc. Mass Spectrom.* **21**, 1753–1761 (2010)
96. Kertesz, T.M., Hall, L.H., Hill, D.W., Grant, D.F.: CE50: quantifying collision-induced dissociation energy for small molecule characterization and identification. *J. Am. Soc. Mass Spectrom.* **20**, 1759–1767 (2009)
97. Hop, C.E.C.A., McMahon, T.B., Willett, G.D.: Determination of bond dissociation energies via energy-resolved collision induced dissociation in a Fourier transform ion cyclotron resonance spectrometer. *Int. J. Mass Spectrom. Ion Process.* **101**, 191–208 (1990)
98. Zhu, Y., Yang, Z., Rodgers, M.T.: Influence of linkage stereochemistry and protecting groups on glycosidic bond stability of sodium cationized glycosyl phosphates. *J. Am. Soc. Mass Spectrom.* **28**, 2602–2613 (2017)
99. Goeringer, D.E., Asano, K.G., McLuckey, S.A.: Ion internal temperature and ion trap collisional activation: protonated leucine enkephalin. *Int. J. Mass Spectrom.* **182**, 275–288 (1999)
100. Huheey, J.E.: The electronegativity of groups. *J. Phys. Chem.* **69**, 3284–3291 (1965)
101. Przybylski, J.L., Wetmore, S.D.: Modeling the dissociative hydrolysis of the natural DNA nucleosides. *J. Phys. Chem. B*. **114**, 1104–1113 (2009)
102. Rios-Font, R., Rodríguez-Santiago, L., Bertran, J., Sodupe, M.: Influence of N7 protonation on the mechanism of the N-glycosidic bond hydrolysis in 2'-deoxyguanosine. A theoretical study. *J. Phys. Chem. B*. **111**, 6071–6077 (2007)
103. Oomens, J., Tielens, A., Sartakov, B.G., von Helden, G., Meijer, G.: Laboratory infrared spectroscopy of cationic polycyclic aromatic hydrocarbon molecules. *Astrophys. J.* **591**, 968–985 (2003)
104. Desiraju, G.M.: The C–H...O hydrogen bond: structural implications and supramolecular design. *Acc. Chem. Res.* **29**, 441–449 (1996)
105. Steiner, T.: The hydrogen bond in the solid state. *Angew. Chem. Int. Ed.* **41**, 48–76 (2002)
106. Grabowski, S.J.: Ab initio calculations on conventional and unconventional hydrogen bonds: study of the hydrogen bond strength. *J. Phys. Chem. A*. **105**, 10739–10746 (2001)